

**The Effect of Shark Skin Inspired Riblet Geometries  
on Drag in Rectangular Duct Flow**

**THESIS**

Presented in Partial Fulfillment of the Requirements for the Degree Master of Science in  
the Graduate School of The Ohio State University

By

Brian Douglas Dean

Graduate Program in Mechanical Engineering

The Ohio State University

2011

Master's Examination Committee:

Professor Bharat Bhushan, Advisor

Professor Shaurya Prakash

## ABSTRACT

The skin of fast swimming sharks exhibits riblet structures aligned in the direction of flow which are known to reduce skin friction drag in the turbulent flow regime. Structures have been fabricated for study and application which replicate and improve upon the natural shape of the shark skin riblets, providing a maximum drag reduction of nearly 10%. Mechanisms of fluid drag in turbulent flow and riblet-drag reduction theories from experiment and simulation are discussed, a review of riblet performance studies performed is given, and optimal riblet geometries for external flow are defined. A survey of studies experimenting with riblet-topped shark scale replicas is also given. A method for selecting optimal riblet dimensions based on fluid flow characteristics is detailed, and current manufacturing techniques are outlined. The effects of mucus and hydrophobicity are presented. A flow cell has been designed for studying riblet effects in internal rectangular duct flow and is discussed. Data collected using several riblet surfaces fabricated for the flow cell is presented and analyzed. A discussion of the effects of the riblets on fluid flow is given, and conclusions are drawn about the possible benefits of riblets in internal fluid flow.

Dedicated to my family and friends, whose support allowed me to succeed

## ACKNOWLEDGEMENTS

I would like to express sincere thanks to my advisor, Professor Bharat Bhushan, for inviting me to work in his research laboratory. Under his guidance, I have been able to achieve to grow my understanding of not only mechanical engineering, but also the world around us. I would also like to give a special thanks to Professor Shaurya Prakash for serving on my examination committee.

My success over the past two years was not a single handed feat, and heartfelt thanks also go out to the Faculty and Staff of the First Year Engineering Department who I worked with throughout my studies—the friendship and support of my colleagues and the instructional staff was integral to my success, all of my colleagues at the NLBB who I have had the privilege of working with and befriending over these past two years, and the faculty and staff in the Mechanical Engineering Department who assisted me on my journey through graduate school.

Most importantly, I would like to thank my family and friends, whose unending support and motivation helped push me through to completion of my degree. The loyalty, support, and kind motivation of my friends, has helped drive me to new heights and pull me through hard times. Lastly, my parents, Cindy and Greg Dean, whose work-ethic, morals, and love have been unwavering, and my siblings Erin and Andrew, who have provided knowledge and guidance; I love you all very much.

## VITA

December 11, 1985 .....Born – Cape Girardeau, MO

2009.....B.S. Mechanical Engineering, The Ohio  
State University, Columbus, OH

2009-2011 .....Graduate Teaching Associate, First Year  
Engineering Department, The Ohio State  
University, Columbus, OH

## FIELDS OF STUDY

Major Field: Mechanical Engineering

## TABLE OF CONTENTS

ABSTRACT.....	ii
ACKNOWLEDGEMENTS.....	iv
VITA.....	v
FIELDS OF STUDY.....	v
TABLE OF CONTENTS.....	vi
LIST OF TABLES.....	viii
LIST OF FIGURES.....	ix
CHAPTER 1 INTRODUCTION.....	14
CHAPTER 2 SHARKSKIN INSPIRED SURFACES FOR FLUID DRAG REDUCTION IN TURBULENT FLOW – A REVIEW.....	18
2.1 Mechanisms of Fluid Drag Reduction.....	18
2.2 Role of Riblets in Drag Reduction.....	23
2.3 Optimization of Riblet Geometries.....	25
2.3.1 Optimization of 2D Riblets.....	27
2.3.2 Studies with 3D Riblets.....	33
2.3.3 Riblet trends in pipe flow.....	36
2.4 Riblet Fabrication and Application.....	39
2.4.1 Riblet dimension selection.....	41
2.4.2 Application of riblets for drag reduction.....	42

2.4.3	Riblet fabrication methods for study and applications.....	45
2.5	Effect of slip length and polymer additives on fluid drag.....	48
2.5.1	The effect of fluid-surface bonding on drag reduction.....	49
2.5.2	Effect of fish mucus and polymers on fluid drag.....	52
2.6	Summary and Outlook.....	55
CHAPTER 3 THE EFFECTS OF SHARK SKIN INSPIRED RIBLET GEOMETRIES		
IN INTERNAL RECTAGULAR DUCT FLOW.....		
3.1	Experimental Design.....	58
3.1.1	Test Setup Design.....	58
3.1.2	Calibration and System Operation.....	62
3.1.3	Riblet Design.....	67
3.1.4	Riblet Fabrication .....	68
3.2	Experimental Results and Discussion.....	72
CHAPTER 4 SUMMARY.....		
LIST OF REFERENCES.....		
		83

## LIST OF TABLES

<b>Table 1</b> Summary and comparison of optimum riblet geometry for various riblet shapes.....	31
---	----

## LIST OF FIGURES

<b>Figure 1</b> Scale patterns on fast-swimming sharks (adapted from Reif, 1985; Bechert et al., 2000a).....	16
<b>Figure 2</b> Transition between laminar and turbulent flow in fluid over a flat plate (adapted from Munson et al., 2005). .....	20
<b>Figure 3</b> Turbulent flow visualization of streamwise vortices in a vertical cross-section over flat-plate and riblet surfaces. All experiments performed using atomized olive oil in air (Adapted from Lee and Lee, 2001).....	22
<b>Figure 4</b> Schematic representation of the mean velocity profiles and effective protrusion heights for flow in both the streamwise direction, $h_{ps}$ , and in the cross flow direction, $h_{pc}$ (adapted from Bechert et al., 1997b). .....	25
<b>Figure 5</b> (a) Schematic representation of riblet dimensions and drag reduction dependence on $\alpha$ for sawtooth riblets. The optimum drag reduction for sawtooth riblets is around $\alpha = 54^\circ$ . For $\alpha = 54^\circ$ , the best-fit line spans two data sets which overlap. (b) Schematic representation of riblet dimensions and drag reduction dependence on $h/s$ ratio for scalloped riblets. The optimum drag reduction for scalloped riblets is around $h/s = 0.7$ . For $h/s = 0.5$ , the best-fit line spans two data sets which overlap. (c) Schematic representation of riblet dimensions and drag reduction dependence on $h/s$ ratio and thickness for blade riblets. Optimum drag reduction for blade riblets occurs at $h/s = 0.5$ . Riblet thickness experiments carried out at $h/s = 0.5$ show thinner riblets provide an improved drag reduction benefit. Blade thickness was changed by inserting thinner blades in place of original blades. All experiments performed using oil as the test fluid	

with the exception of the  $\alpha = 54^\circ$  by Walsh who tested in air. (adapted from Walsh, 1982; Bechert et al., 1997b).....27, 28, 30

**Figure 6** (a) Drag reduction comparison for sawtooth, scalloped, and blade riblets with  $h/s = 0.5$ . All experiments performed using oil as the test fluid. (b) Schematic representations of lines of constant velocity above riblet and flat-plate surfaces in laminar flow allow for a comparison of effective protrusion height,  $h_p$ , of sawtooth, scalloped, and blade riblets. The effective protrusion height, which is favorable for the reduction of vortex translation reduction, is the difference between the riblet height,  $h$ , and the upward shift in the effective flow origin,  $\Delta_0$ ;  $h_p = \Delta_0 - h$ . To find the upward shift in the effective flow origin, the height and velocity of the lowest undisturbed line of constant velocity above a riblet surface are determined. Next, the height at which flow over a flat-plate reaches the same velocity is determined. The difference between these two heights is the upward shift in the effective flow origin. Blade riblets have the largest effective protrusion height. Scalloped riblets have the second largest, and sawtooth riblets have the lowest of the three (adapted from Bechert et al., 1986, 1997b). .....31, 32

**Figure 7** Drag reduction dependence on yaw angle,  $\beta$ , of sawtooth riblets in free stream for  $h/s \approx 0.62$ . All experiments performed using air as the test medium (adapted from Walsh and Lindemann, 1984).....34

**Figure 8** Comparison of drag reduction over optimum continuous blade riblets with optimum segmented trapezoidal blade riblets. (a) Segmented riblets were staggered as shown. Spacing between offset rows is  $s/2$ , while spacing between corresponding rows is  $s$ . (b) Optimal  $h/s$  ratio for staggered blade riblets is 0.4. Staggered blade riblets provide

less drag reduction benefit than continuous blade riblets. All experiments performed using oil as the test fluid (Adapted from Bechert, et al., 1997b, 2000a). .....35

**Figure 9** (a) SEM micrographs of shark skin replica patterned in epoxy. (b) Segmented bade-style riblets fabricated from acrylic. (Jung and Bhushan, 2010). .....37

**Figure 10** (a) Comparison of pressure drop in rectangular pipe flow over flat epoxy surface with shark skin replica surface. (b) Comparison of pressure drop in rectangular pipe flow over flat acrylic surface and segmented blade riblets. Data are compared with the predicted pressure drop function for a hydrophilic surface. All experiments performed using water as the test fluid (adapted from Jung and Bhushan, 2010).....38

**Figure 11** Comparison of riblet performance curves over sawtooth riblets on a flat-plate surface and inside round pipes of 25.4 mm and 50.8 mm diameters. Peak drag reduction for riblets in pipe flow occurs near  $s^+ = 12$ , which is lower than the flat plate optimal value of  $s^+ = 15$ . Bechert experiments performed using oil as the test fluid, and Liu experiments performed using water as the test fluid (adapted from Liu, et al., 1990; Bechert et al., 1997b). .....40

**Figure 12** Images of riblet geometries on (a) unstretched and (b) stretched Speedo FastSkin® swimsuit. (c) Schematic showing apparent hierarchical riblet structure formed by threads. ....44

**Figure 13** Comparison of drag reduction with oil and air on similar sawtooth surfaces (adapted from Walsh, 1982; Bechert et al., 1997b).....49

**Figure 14** Schematic of velocity profiles with and without boundary slip. Slip length,  $b$ , occurs on hydrophobic surfaces (Jung and Bhushan, 2010).....50

**Figure 15** Comparison of pressure drop in pipe flow of hydrophilic, hydrophobic, and superhydrophobic surfaces in laminar and turbulent flow regimes. Decreased pressure drop in pipe flow corresponds to decreased drag (adapted from Jung and Bhushan, 2010).....51

**Figure 16** (a) Behavior of hydrophilic surface in fluid flow. (b) Proposed deposition of hydrophobic surface on portions of blade riblet surface should increase the protrusion height of riblets and increase drag reduction benefit.....54

**Figure 17** Schematic representation of experimental setup showing the pump, test loop, bypass loop, and return. The test loop consists of a control valve for varying flow velocity, a rotameter for measuring flow rate, a differential pressure transducer, and the flow cell with the riblet test section shown. The bypass loop consists of only a resistance valve, which is used prior to all experimentation to adjust the flow rate limits of the system within the pumps working pressure range. ....59

**Figure 18** (a) Pressure drop comparison between theoretical and experimental flat plate surfaces in a 4 cm x 1 cm channel demonstrating viability of the system. (b) Pressure drop comparison between theoretical and experimental flat plate surfaces in a 3 cm x 1 cm channel demonstrating viability of the system. ....65

**Figure 19** Microscope visualization of milled riblet surface. Dark lines are raised blade riblets, and lighter areas with swirl marks are milled valleys. Some amount of roughness is evident at the corners of each riblet peak as well as in the riblet valleys. ....69

**Figure 20** Pressure drop comparison over riblet surfaces with various h/s ratios and flat plate surfaces in a (a) 4cm x 1cm channel and (b) 3cm x 1cm channel. ....73

**Figure 21** Pressure drop comparison over  $h/s = 0.3$  riblets and flat plate surface in a (a) 4 cm x 1 cm channel and (b) 3 cm x 1 cm channel. Pressure drop comparison over  $h/s = 0.5$  riblets and flat plate surface in a (c) 4 cm x 1 cm channel and (d) 3 cm x 1 cm channel. Pressure drop comparison over  $h/s = 0.7$  riblets and flat plate surface in a (e) 4 cm x 1 cm channel and (f) 3 cm x 1 cm channel. ....74

**Figure 22** Pressure drop comparison over flat plate surface and riblets with  $h/s = 0.5$  and varied riblet spacing in a 3cm x 1cm channel. ....75

**Figure 23** (a) Pressure drop comparison over  $h/s = 0.5$  riblets with 254 $\mu$ m spacing and flat plate surface in a 3cm x 1cm channel. (b) Pressure drop comparison over  $h/s = 0.5$  riblets with 356 $\mu$ m spacing and flat plate surface in a 3cm x 1cm channel. (c) Pressure drop comparison over  $h/s = 0.5$  riblets with 508 $\mu$ m spacing and flat plate surface in a 3cm x 1cm channel. ....77

## CHAPTER 1

### INTRODUCTION

Nature is full of examples of structures, materials, and surfaces that can benefit science and humanity. The field of design inspired by biologically natural traits is known as biomimetics. By studying and understanding the mechanisms of natural phenomena, we may be able to recreate these phenomena on demand (Bhushan, 2009). Efficient design is a common trait in nature, and many structures serve multiple purposes. Lotus leaves, one example of a surface with natural traits desirable in other applications, possess a surface structure that causes superhydrophobic behavior (Bhushan, 2008, 2010; Nosonovsky and Bhushan, 2008). This allows for low skin friction when in contact with liquids, which allows any dirt particles on the surface to be swept away by rainwater. Rose petals are found with superhydrophobicity and either low or high adhesion (Bhushan and Her, 2010). Geckos, which can walk up walls and hang upside down, also possess a hierarchical structure giving them controllable super-adhesion on their feet (Gorb, 2001; Bhushan, 2007, 2010). By creating these directional super-adhesive surfaces on legs of a robot, it is possible to create a robot which can climb walls like a Gecko (Cutkosky and Kim, 2009).

Nature has also created ways of reducing drag in fluid flow, evident in the efficient movement of fish, dolphins, and sharks. The mucus secreted by fish causes a

reduction in drag as they move through water, and also protects the fish from abrasion by making the fish slide across objects rather than scrape and disease by making the surface of the fish difficult for microscopic organisms to adhere to (Shephard, 1994). It has been known for many years that by adding as little as a few hundred parts per million guar, a naturally occurring polymer, friction in pipe flow can be reduced by up to two-thirds. Other synthetic polymers provide an even larger benefit (Hoyt, 1975). The compliant skin of the dolphin has also been studied for drag reducing properties. By responding to the pressure fluctuations across the surface, a compliant material on the surface of an object in a fluid flow has been shown to be beneficial. Though early studies showed dramatic drag reduction benefits, later studies have only been able to confirm 7% drag reduction (Choi et al., 1997).

Another set of aquatic animals which possesses multi-purpose skin is fast swimming sharks. The skin of fast swimming sharks protects against biofouling and reduces the drag experienced by sharks as they swim through water. The tiny scales covering the skin of fast swimming sharks, known as dermal denticles (skin teeth), are shaped like small riblets and aligned in the direction of fluid flow (Fig. 1). Shark skin inspired riblets have been shown to provide a drag reduction benefit up to 9.9% (Bechert et al., 1997b). The spacing between these dermal denticles is such that microscopic aquatic organisms have difficulty adhering to the surface. Slower sharks are also covered in dermal denticles but not those shaped like riblets or provide drag reduction benefit.

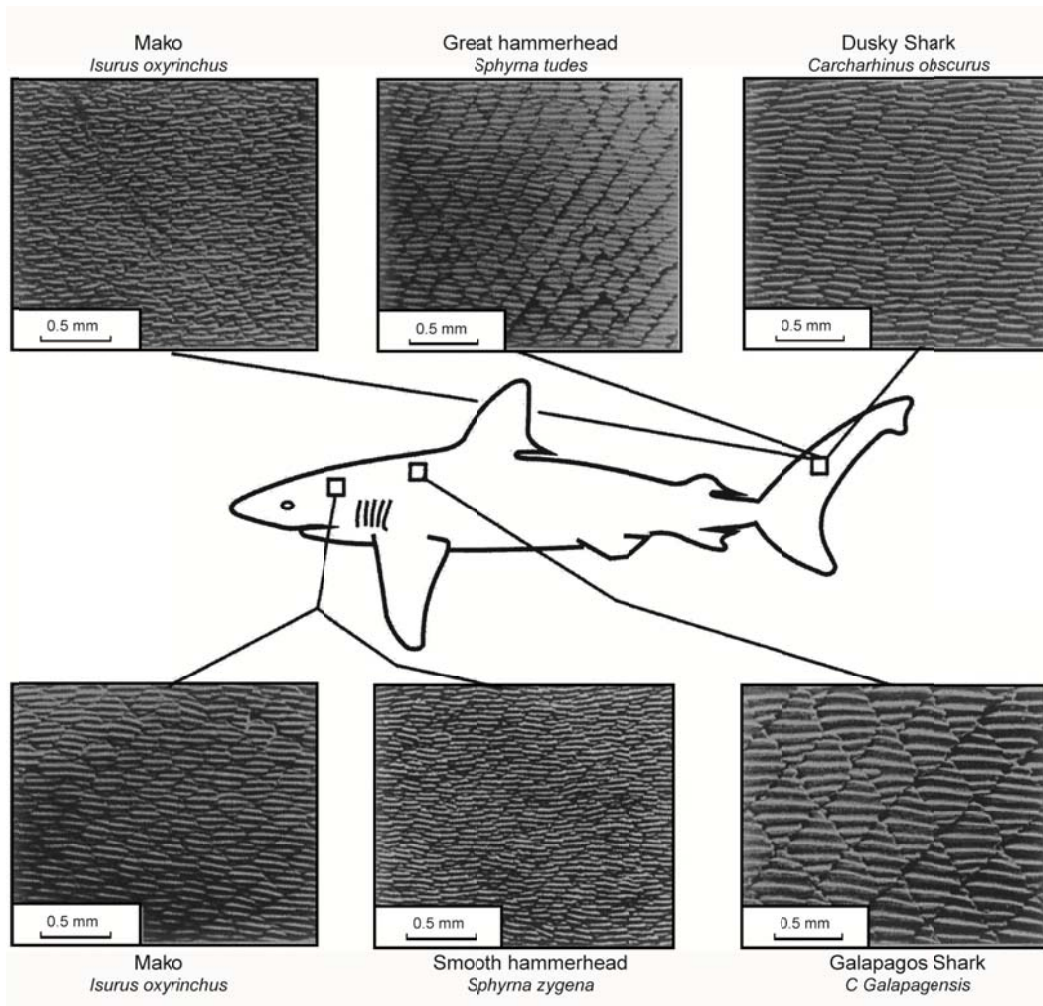


Figure 1 Scale patterns on fast-swimming sharks (adapted from Reif, 1985; Bechert et al., 2000a).

The effect of riblet structures in internal rectangular duct flow is the focus of this paper. To understand the mechanism of shark skin drag reduction, it is first important to understand the nature of fluid flow over an effective shark skin surface. Flow characteristics and the mechanism of fluid drag will be discussed for fluid flowing over a flat plate. Mechanisms of drag reduction by riblet geometries will then be discussed, followed by a review of experimental riblet studies which have been performed in

external flow, a discussion of optimization data for common riblet geometries, and other factors in riblet selection. Large-scale and commercial applications of riblets will then be explored, and an outlook on future research in the field will be presented.

The application of riblets in internal rectangular duct flow will then be explored in terms of the effect which riblets have on the pressure drop across a test section due to the interaction of the riblets with structures within the turbulent flow. In external flow, drag is an important quantity to understand, and most studies in external flow relate the benefit of riblets to either drag or shear stress on the surface. Both of these quantities can be thought of interchangeably for application, as they are directly proportional. In internal flow applications, pressure drop is an equivalent measure, and data and discussion will be in terms of pressure drop comparisons rather than drag or shear stress.

## CHAPTER 2

### SHARK SKIN INSPIRED SURFACES FOR FLUID DRAG REDUCTION IN TURBULENT FLOW – A REVIEW

#### 2.1 Mechanisms of Fluid Drag

Fluid drag comes in several forms, the most basic of which are pressure drag and friction drag. Pressure or form drag is the drag associated with the energy required to move fluid out from in front of an object in the flow, and then back in place behind the object. Much of the drag associated with walking through water is pressure drag, as the water directly in front of a body must be moved out and around the body before the body can move forward. The magnitude of pressure drag can be reduced by creating streamlined shapes. Friction or viscous drag is caused by the interactions between the fluid and a surface parallel to the flow, as well as the attraction between molecules of the fluid. Friction drag is similar to the motion of a deck of cards sliding across a table. The frictional interactions between the table and the bottom card as well as between each successive card mimic the viscous interactions between molecules of fluid. Moving away from the surface of an object in a fluid flow, each fluid layer has less velocity until a layer is reached where the fluid has zero velocity. Fluids of higher viscosity—the attraction between molecules—have higher apparent friction between fluid layers, which increases the thickness of the fluid layer distorted by an object in a fluid flow. For this reason, more viscous fluids have relatively higher drag than less viscous fluids. A similar

increase in drag occurs as fluid velocity increases. The drag on an object is in fact a measure of the energy required to transfer momentum between the fluid and the object to create a velocity gradient in the fluid layer between the object and undisturbed fluid away from the object's surface.

The above discussion of friction drag assumes all neighboring fluid molecules move in the same relative direction and momentum transfer occurs between layers of fluid flowing at different velocities. Figure 2 shows an image of the transition between laminar flow and turbulent flow, in which molecules move in swirling and cross-stream motions such that an average velocity is maintained in the direction of flow. The inclusion of cross-flow and non-parallel relative velocities between molecules in turbulent flow causes a dramatic increase in momentum transfer. The cross-flow momentum transfer is of particular interest, as all momentum transferred parallel to the surface of an object results in a corresponding increase in drag. Natural transition occurs from laminar to turbulent flow regimes near a Reynolds number around 4000 for pipe flow and 500,000 for flow over a flat plate. Reynolds number,  $Re$ , is a ratio of the inertial forces to viscous forces in a given flow. For pipe flow,  $Re = \rho VD/\mu$ , where  $\rho$  = fluid density,  $V$  = velocity,  $D$  = pipe diameter, and  $\mu$  = dynamic viscosity. For flow over a flat plate,  $Re = \rho VL/\mu$ , where  $L$  = length. For values of  $Re$  much less than the transition values above, flow is laminar—dominated by viscous forces between the molecules. For larger values of  $Re$ , the flow is turbulent—dominated by inertial forces of the system (Munson et al., 2005).

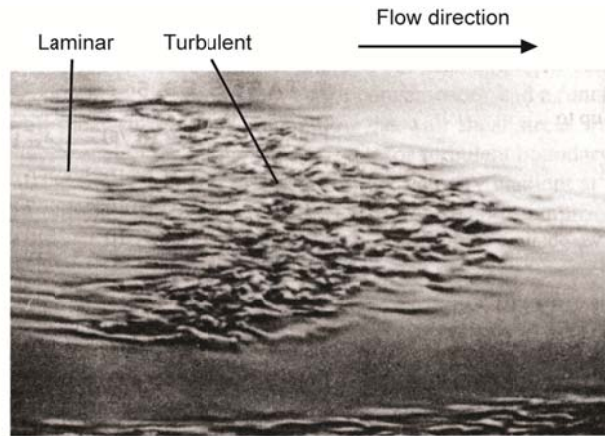


Figure 2. Transition between laminar and turbulent flow in fluid over a flat plate (adapted from Munson et al., 2005).

Fully developed turbulent flow is commonly said to exhibit complete randomness in its velocity distribution, but there exist distinct regions within fully developed turbulent flow that exhibit different patterns and flow characteristics (Kline et al., 1967). While organization is evident in the viscous sublayer, the layer closest to the surface, the outer layers of the turbulent boundary layer are chaotic and disorganized. Much of this chaotic motion above the viscous sublayer is caused by the outward ejection of the streamwise vortices that form at the surface in the viscous sublayer. Streamwise vortices (vortices which rotate about axes in the direction of mean velocity) dominate the viscous sublayer. As these vortices rotate and flow along the surface, they naturally translate across the surface in the cross-flow direction. The interaction between the vortices and the surface, as well as between neighboring vortices that collide during translation initiate ejection motions where vortices are rapidly ejected from the surface and into the outer boundary layers. As vortices are ejected, they tangle with other vortices and twist such that transient velocity vectors in the cross-stream direction can become as large as those

in the average flow direction (Kline et al., 1967). The translation, ejection of vortices out of the viscous sublayer, and chaotic flow in the outer layers of the turbulent boundary layer flow are all forms of momentum transfer and are large factors in fluid drag. Reducing the ejection behavior of the streamwise vortices is a critical goal of drag reduction, as the drag reduction possibilities presented by this are sizable.

The vortices were first visualized from a horizontal cross section and were seen as high and low speed streaks aligned in the mean flow direction (Coles, 1978). Later, a full Navier-Stokes simulation was used to replicate the high and low speed streaks (Robinson, 1991), and more recently flow visualization techniques were used to capture cross sectional images, shown in figure 3, of the streamwise vortex formations above both flat-plate and riblet surfaces (Lee and Lee, 2001). The streaky structure that was seen in the horizontal cross section was representative of local average velocity flows, and is caused by the interactions between the interactions neighboring vortices. The average cross-stream wavelength of these high and low speed streaks, the added widths of one high speed streak and one low speed streak, is equal to the added diameters of two neighboring vortices and has been measured at 70–100 wall units<sup>1</sup> (Kline et al., 1967; Wilkinson, 1983; Bechert et al., 2000a). This corresponds to a vortex diameter of 35-50 wall units.

---

<sup>1</sup> As flow properties change, the dimensions of the turbulent flow structures change as well. As such, it is useful to use non-dimensional length values to better compare studies performed in different flow conditions. Dimensionless wall units, marked <sup>+</sup>, are used for all length scales, which are calculated by multiplying the dimensional length by  $V_\tau/\nu$ . For example,  $s^+ = sV_\tau/\nu$ , where  $s^+$  is the nondimensional riblet spacing,  $s$  is the dimensional riblet spacing,  $\nu$  is the kinematic viscosity, and  $V_\tau = (\tau_0/\rho)^{0.5}$  is the wall stress velocity, for which  $\rho$  is the fluid density and  $\tau_0$  is the wall shear stress. Wall shear stress can be estimated for round pipe flow using the equation  $\tau_0 = 0.03955V^{1/4}\rho V^{7/4}d^{-1/4}$ , where  $V$  is the average flow velocity and  $d$  is the hydraulic diameter. For flow in rectangular pipes, the equation for hydraulic diameter  $d = 4A/c$  can be applied, where  $A$  is the cross sectional area and  $c$  is the wetted perimeter.

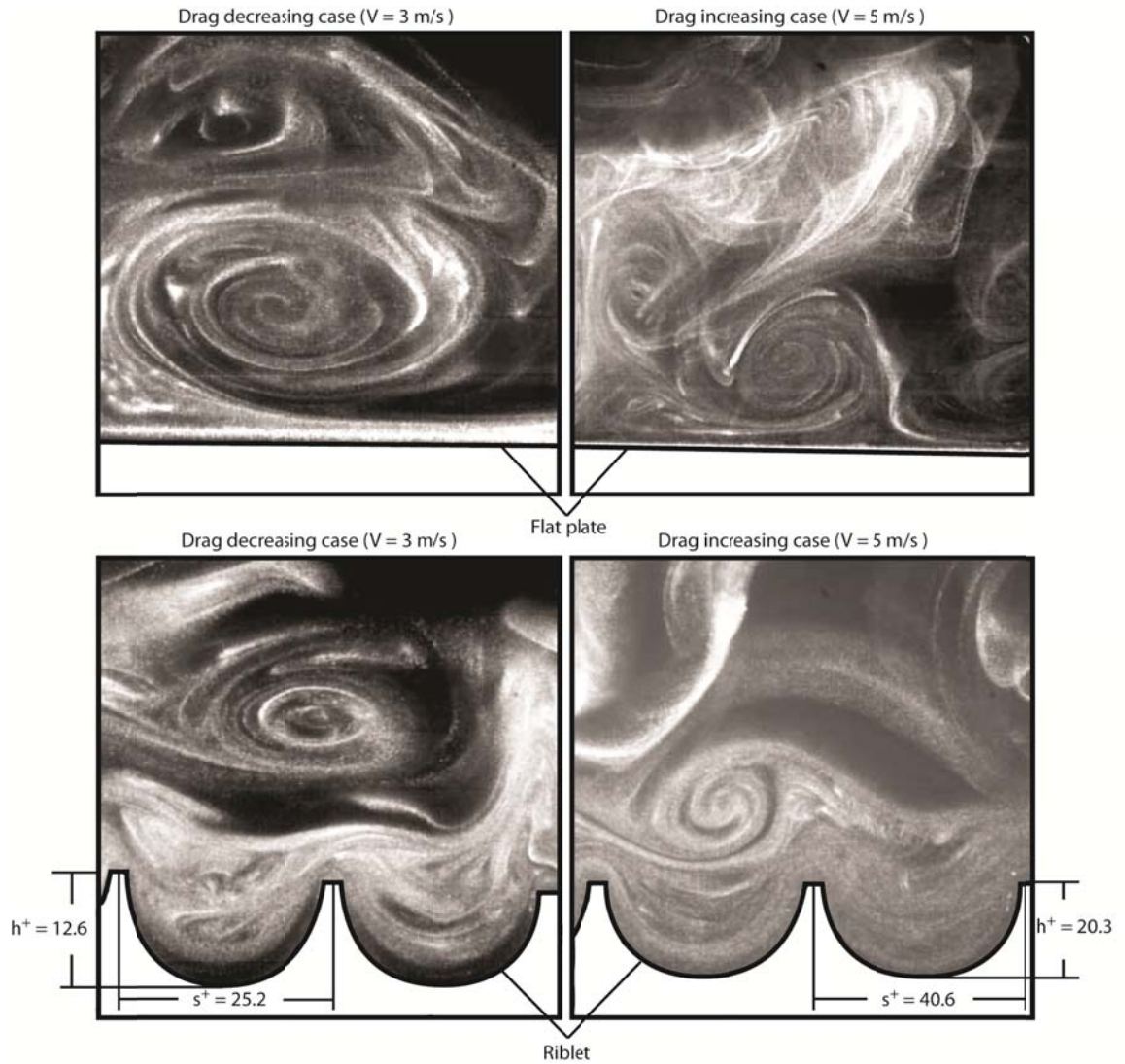


Figure 3. Turbulent flow visualization of streamwise vortices in a vertical cross-section over flat-plate and riblet surfaces. All experiments performed using atomized olive oil in air (Adapted from Lee and Lee, 2001).

Flow visualizations shown in figure 3 show vortex cross sections and relative length scales, demonstrating vortex diameters smaller than 40 wall units (Lee and Lee, 2001).

## **2.2 Role of riblets in drag reduction**

The small riblets that cover the skin of fast swimming sharks work by decreasing the total shear stress across the surface and by impeding the cross-stream translation of the streamwise vortices in the viscous sublayer. While these effects and their role in the final reduction of drag are understood and reproducible, the underlying mechanisms which cause the reduction in vortex translation are not fully understood.

One classical cause of increased drag that shark skin-mimicking riblet surfaces exhibit is an increase in wetted surface area. In the turbulent flow regime, fluid drag typically increases dramatically with an increase in surface area due to the shear stresses at the surface acting across the new, larger surface area. However, as vortices form above a riblet surface, they remain above the riblets, interacting with the tips only and rarely causing any high-velocity flow in the valleys of the riblets. Since the higher velocity vortices interact only with a small surface area at the riblet tips, only this localized area experiences high shear stresses. The low velocity fluid flow in the valleys of the riblets produces very low shear stresses across the majority of the surface of the riblet. By keeping the vortices above the riblet tips, the cross-stream velocity fluctuations inside the riblet valleys are much lower than the cross-stream velocity fluctuations above a flat plate (Lee and Lee, 2001). This difference in cross-stream velocity fluctuations is evidence of a reduction in shear stress and momentum transfer near the surface, which minimizes the effect of the increased surface area. Though the vortices remain above the riblet tips, some secondary vortex formations do occur that enter the riblet valleys transiently. The flow velocities of these transient secondary vortices are such that the

increase in shear stress caused by their interaction with the surface of the riblet valleys is small.

Protruding into the flow without greatly increasing fluid drag allows the riblets to interact with the vortices to reduce the cross-stream translation and related effects. As the riblets protrude into the flow field, they raise the effective flow origin by some distance. The amount by which the height of the riblets is greater than the apparent vertical shift of the flow origin is referred to as the effective protrusion height. By calculating the average streamwise velocity in laminar flow at heights over riblet surfaces and comparing them to the average streamwise velocities in laminar flow at heights over a flat plate, the effective streamwise protrusion height,  $h_{ps}$ , is found for laminar flow. The effective cross-stream protrusion height,  $h_{pc}$ , is similarly found for laminar flow by comparing the cross-stream velocities over a riblet surface to those over a flat plate. A schematic of streamwise and cross-stream flow velocity profiles and effective protrusion heights is shown in figure 4. The difference between the vertical shifts in the streamwise and cross-stream origin,  $\Delta h = h_{ps} - h_{pc}$ , for any riblet geometry has been proposed to be the degree to which that riblet geometry will reduce vortex translation for low Re flows (Bechert et al., 1997b). As Re increases, the degree to which increased surface area affects the overall fluid drag increases, and the drag reduction correlation to these laminar flow theories deteriorates.

The second mechanism of drag reduction which riblets are known to provide is a reduction in non-streamwise momentum transfer. Though the underlying mechanisms are not completely understood, the riblets which protrude into the flow cause an increase

in cross-flow shear stress (Bechert et al., 1997b). This in turn causes a reduction in cross-flow vortex translation, which decreases vortex interaction, ejection, and outer layer turbulence. The momentum carried in ejected vortices and transferred in non-streamwise directions is purely wasteful to the efficiency of the flow, and by reducing the translation and ejection of vortices on the surface, large gains in energy efficiency can be made.

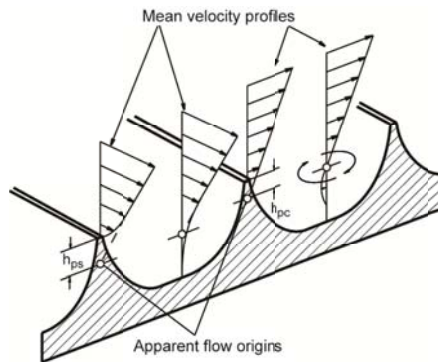


Figure 4. Schematic representation of the mean velocity profiles and effective protrusion heights for flow in both the streamwise direction,  $h_{ps}$ , and in the cross flow direction,  $h_{pc}$  (adapted from Bechert et al., 1997b).

### 2.3 Optimization of riblet geometry

The cross sectional shape of riblets on fast swimming sharks varies greatly, even at different locations on the same shark. Figure 1 shows the difference between the separated blade riblets on the tail of a Mako with the scale-grouped riblets on its front section, as well as the morphology that exists on various other fast swimming sharks. Because of the variance in nature, a wide variety of synthetic riblets have also been characterized. Two-dimensional (2D) riblets, which have a continuous extrusion of a simple cross section in the streamwise direction, have been most extensively

characterized. The most thorough characterization has been completed for symmetrical 2D riblets with sawtooth, scalloped, and blade cross sections as shown in figure 5 (Walsh, 1980, 1982; Bechert and Hoppe, 1985; Bechert et al., 1986, 1997a, 2000a, b;; Walsh and Lindemann 1984; Wilkinson and Lazos, 1987; Wilkinson et al., 1988; Walsh and Anders, 1989). Alternative riblet geometries have, in general, shown no increased benefit. These riblets, including asymmetrical riblets, hierarchical riblets, and riblets with rounded or notched peaks have been studied in detail and do not improve upon the benefit of standard riblet geometries (Walsh, 1980, 1982; Walsh and Lindemann, 1984). Other 2D riblet shapes which have been studied include alternating brother-sister type riblets (Bechert et al., 1997a) and hierarchical riblets with small riblets on top of larger riblets (Wilkinson et al., 1987). Three-dimensional (3D) riblets, which include segmented 2D riblets as well as shark skin moldings and replicas have also been studied. Riblet types characterized include aligned segmented-blade riblets (Wilkinson and Lazos, 1987), offset segmented-blade riblets (Bechert et al., 2000a), offset-3D blade riblets (Bechert et al., 2000a), and 3D shark skin replicas (Bechert et al., 2000b; , Lang et al., 2008; Jung and Bhushan, 2010).

Most studies are done by changing the non-dimensionalized spacing,  $s^+$ , by varying only fluid velocity and collecting shear stress data from a shear stress balance in a wind tunnel or fluid flow channel. Pipe flow tests will be discussed as well. Measured shear stress is compared to shear stress over a flat plate and plotted against the calculated  $s^+$  value for the flow conditions. In this manner, a performance curve is created for a riblet array with a specific set of characteristic dimensions. Experiments have been

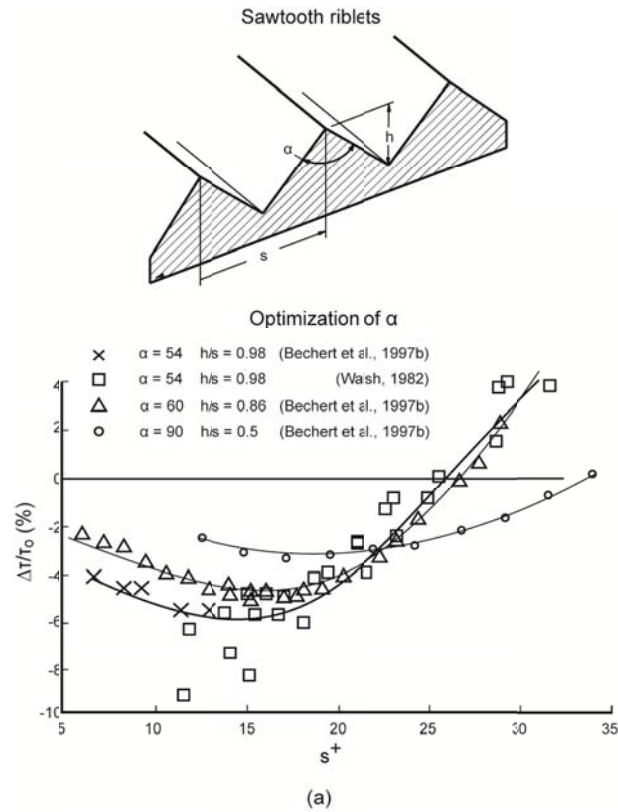


Figure 5(a). Schematic representation of riblet dimensions and drag reduction dependence on  $\alpha$  for sawtooth riblets. The optimum drag reduction for sawtooth riblets is around  $\alpha = 54^\circ$ . For  $\alpha = 54^\circ$ , the best-fit line spans two data sets which overlap All experiments performed using oil as the test fluid with the exception of the  $\alpha = 54^\circ$  by Walsh who tested in air. (adapted from Walsh, 1982; Bechert et al., 1997b).

carried out with various surface materials and in air, oil, and water. Under the same non-dimensionalized flow conditions, riblet arrays sharing characteristic dimension ratios create similar performance curves whether they are made of different materials, are tested in different fluids, or a fabricated at a different scale.

### 2.3.1 Optimization of 2D riblets

Sawtooth riblets are the most commonly studied riblets. A schematic with characteristic dimensions and optimization data are shown in figure 5a. Sawtooth riblets

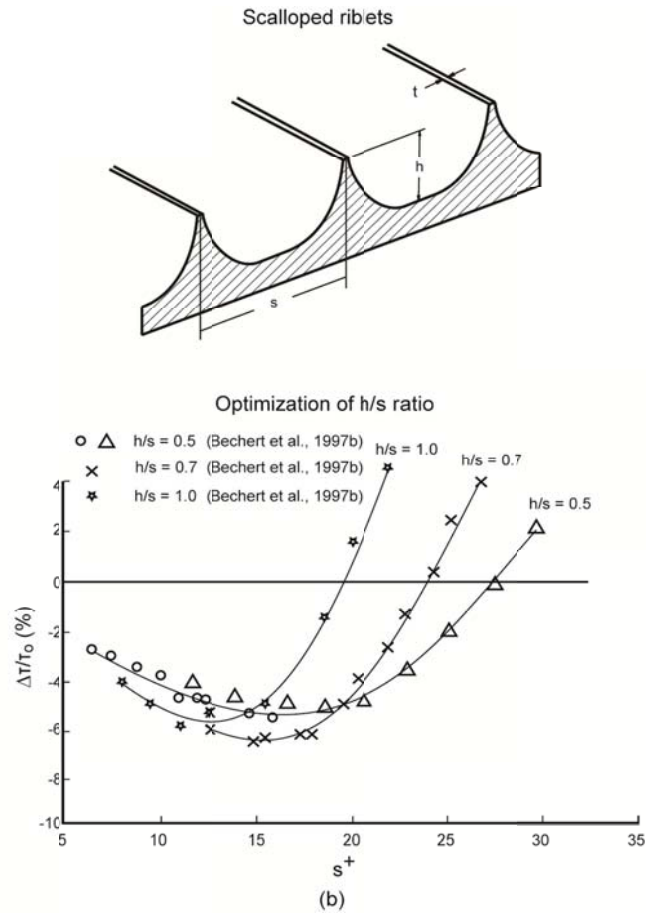


Figure 5(b). Schematic representation of riblet dimensions and drag reduction dependence on  $h/s$  ratio for scalloped riblets. The optimum drag reduction for scalloped riblets is around  $h/s = 0.7$ . For  $h/s = 0.5$ , the best-fit line spans two data sets which overlap. All experiments performed using oil as the test fluid (adapted from Bechert et al., 1997b)

are defined either by their height-to-spacing ( $h/s$ ) ratio or their peak angle,  $\alpha$ . Figure 5a shows the optimization data for sawtooth riblets. The best-fit line for riblets with  $\alpha \sim 54^\circ$  was drawn spanning overlapping data sets from different sources. From available data, the optimal sawtooth riblets provide about 5% drag reduction at  $h/s \sim 1.0$  and  $\alpha = 54^\circ$  (Bechert et al., 1997b).

Scalloped riblets are most commonly defined by their  $h/s$  ratio, but test shapes have varied between research groups. While the basic shapes are similar, no consensus has been formed about a standard scalloped profile. Generally, any concave shape may be referred to as scalloped, and comparing data between sawtooth, scalloped, and blade riblet optimizations will support a generalization of comparable shapes. Ideally, the tip of the riblet is thin and sharp, but scalloped riblets with measurable tip thicknesses have also produced favorable results. Figure 5b shows optimization data for scalloped riblets. A maximum drag reduction of 6.5% has been achieved for scalloped riblets with  $h/s \sim 0.7$  (Bechert et al., 1997b).

Blade riblets have been rigorously studied in their characteristic dimension ratios. A schematic with characteristic dimensions and optimization data for blade riblets is in figure 5c. By fabricating an adjustable blade riblet test stand, 9.9% drag reduction was achieved with optimized dimensions of  $h/s \sim 0.5$  and  $t/s = 0.02$  were found (Bechert et al., 1997b). Due to their inherent weak structure, optimal blade riblet thickness is limited by strength, not fluid dynamics. Blades that are too thin will warp in fluid flow and allow vortices to translate as a result.

When comparing the optimal drag reduction geometries for sawtooth, scalloped, and blade riblets shown in figure 6a, it is clear that blade riblets provide the highest level of drag reduction, scalloped riblets provide the second most, and sawtooth riblets provide the least benefit. A summary of comparison features for sawtooth, scalloped, and blade riblets is provided in table 1. In general, it can be seen in figure 5 that each type of riblets is most beneficial near  $s^+ \sim 15$ , which is between  $1/3$  and  $1/2$  the width of the streamwise

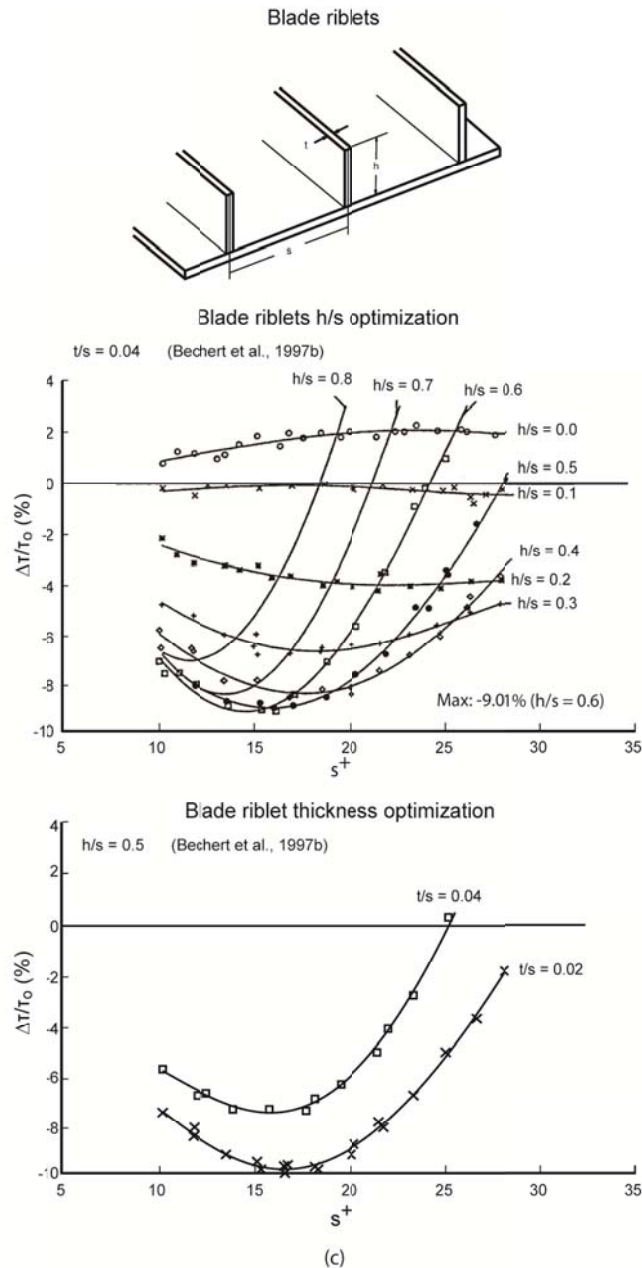


Figure 5(c). Schematic representation of riblet dimensions and drag reduction dependence on  $h/s$  ratio and thickness for blade riblets. Optimum drag reduction for blade riblets occurs at  $h/s = 0.5$ . Riblet thickness experiments carried out at  $h/s = 0.5$  show thinner riblets provide an improved drag reduction benefit. Blade thickness was changed by inserting thinner blades in place of original blades. All experiments performed using oil as the test fluid (adapted from Bechert et al., 1997b).

vortices. Larger  $s^+$  will cause vortices to begin falling into the gap between the riblets, which increases the shear stress at the surface between riblets. As  $s^+$  decreases below optimum, the overall size of the riblets decreases to a point below which they cannot adequately impede vortex translation.

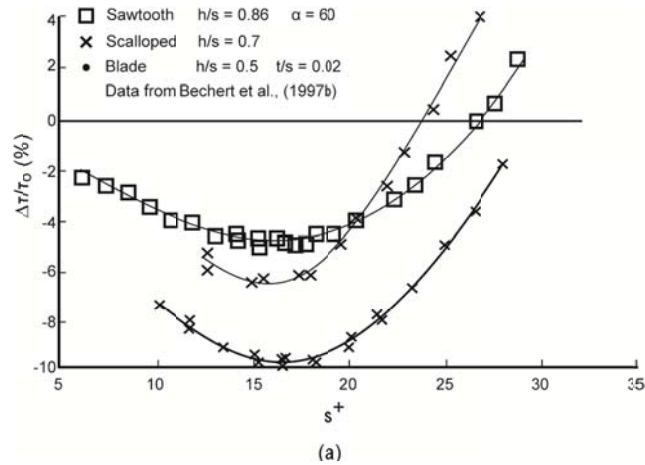


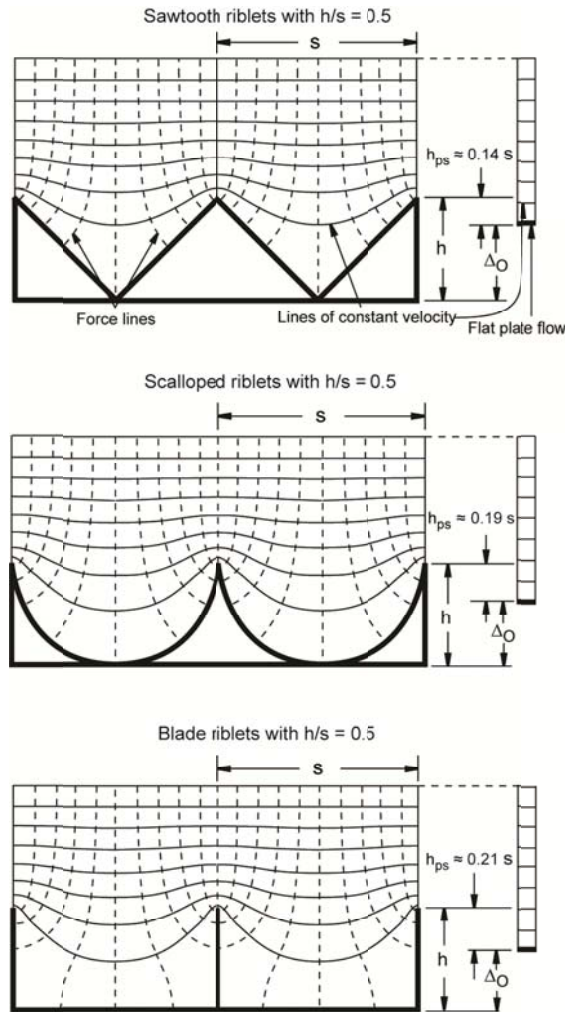
Figure 6. (a) Drag reduction comparison for sawtooth, scalloped, and blade riblets with  $h/s = 0.5$ . All experiments performed using oil as the test fluid (adapted from Bechert et al., 1986, 1997b)

Table 1. Summary and comparison of optimum riblet geometry for various riblet shapes.

Riblet shape	Relative rank*	Maximum drag reduction**	Optimum geometry**	Comments
Sawtooth	3	5%	$h/s \sim 1, \alpha \sim 60^\circ$	Most durable
Scalloped	2	6.5%	$h/s \sim 0.7$	
Blade	1	9.9%	$h/s \sim 0.5$	Drag reduction increases as riblet thickness decreases. Durability is an issue.

\* 1 corresponds to greatest drag reduction

\*\* based on published data in Bechert et al., 1997b



(b)

Figure 6(b) Schematic representations of lines of constant velocity above riblet and flat-plate surfaces in laminar flow allow for a comparison of effective protrusion height,  $h_p$ , of sawtooth, scalloped, and blade riblets. The effective protrusion height, which is favorable for the reduction of vortex translation reduction, is the difference between the riblet height,  $h$ , and the upward shift in the effective flow origin,  $\Delta_O$ ;  $h_p = \Delta_O - h$ . To find the upward shift in the effective flow origin, the height and velocity of the lowest undisturbed line of constant velocity above a riblet surface are determined. Next, the height at which flow over a flat-plate reaches the same velocity is determined. The difference between these two heights is the upward shift in the effective flow origin. Blade riblets have the largest effective protrusion height. Scalloped riblets have the second largest, and sawtooth riblets have the lowest of the three (adapted from Bechert et al., 1986, 1997b).

Comparing drag reduction benefit potential to effective protrusion height in the streamwise direction, it is apparent that increased protrusion height is correlated to drag reduction potential. Figure 6b shows the effective streamwise protrusion height for sawtooth, scalloped and blade riblets. For the same  $h/s$ , blade riblets have the smallest shift in the effective flow origin due to their small cross sectional area, and sawtooth have the largest shift in the effective flow origin. Though all three profiles share a calculated maximum streamwise protrusion height of 0.2206  $s$  at separate values of  $h/s$ , an increase in overall drag is experienced at these values due to the increased drag contributions of surface shear stress effects on the increased surface area in the turbulent regime (Bechert et al., 1986). The height at which  $h_p$  is maximized causes such an increase in effective flow origin shift that the drag reduction benefits are outweighed.

An additional concern to the application of riblets is the sensitivity of drag reduction to yaw angle. Yaw angle, the angle between the average flow direction and the riblet orientation, has a deleterious effect on the drag reduction benefits of riblet surfaces. Riblet surfaces become drag inducing above  $\beta = 30^\circ$ , but small drag reductions can still be seen up to  $\beta = 15^\circ$  (Walsh and Lindemann, 1984). Figure 7 shows the effects of yaw angle on riblet performance for flow over sawtooth riblets.

### 2.3.2 *Studies with 3D riblets*

Riblets on shark skin exist in short segments and groups, not as continuous structures. Riblets with 3D features have been created to better approximate the performance of actual shark skin and to determine if there are methods of drag reduction not yet understood from 2D riblet studies. Studies have explored the effects of

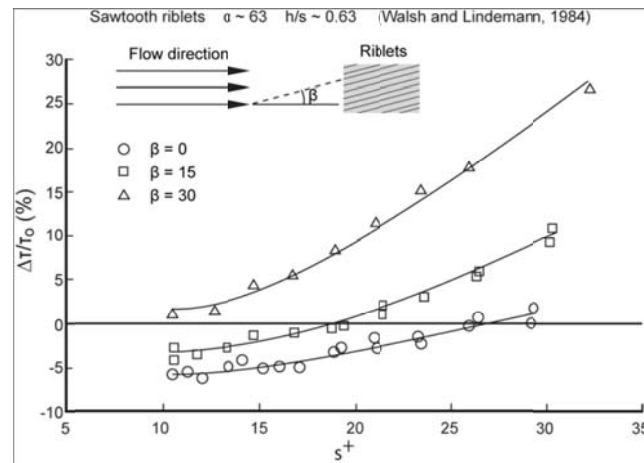
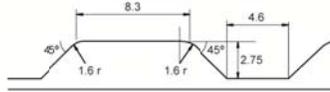
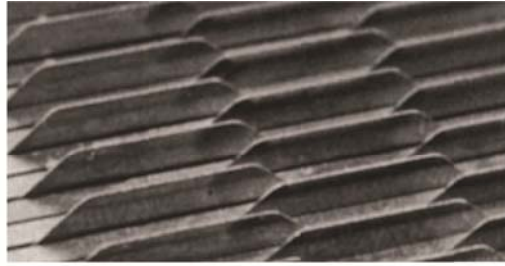
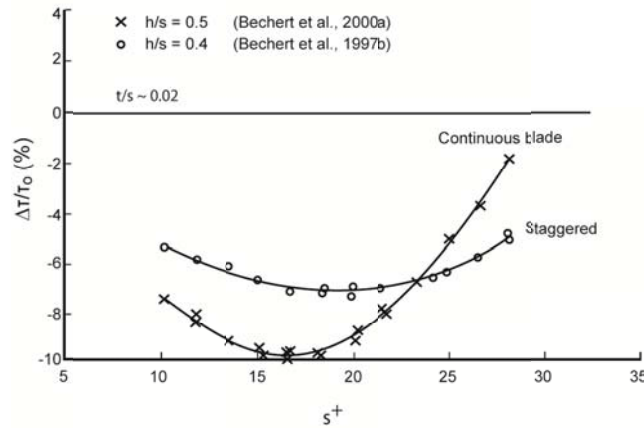


Figure 7. Drag reduction dependence on yaw angle,  $\beta$ , of sawtooth riblets in free stream for  $h/s \approx 0.62$ . All experiments performed using air as the test medium (adapted from Walsh and Lindemann, 1984).

compound riblet structures and 3D riblets comprised of aligned, segmented-blade riblets (Wilkinson et al., 1988). No improvement in net drag reduction was realized when compared to corresponding performance of continuous riblet geometries. More recently, experiments with similarly shaped segmented blade riblets at spacing  $s$  with a matching set of segmented blade riblets staggered between each row of blades at a spacing of  $s/2$  from either side have been performed (Bechert et al., 1997b). A schematic and image of the staggered trapezoidal blade riblets is shown in figure 8a. Using these and other staggered riblets, Bechert et al. (1997b) hoped to achieve the same vortex elevation and anti-translation effects of continuous riblets with less effect on the flow origin. Experimental data comparing the largest drag reduction achieved with staggered segmented blade riblets to optimum continuous blade riblets can be seen in figure 8b. No net benefit in drag reduction was achieved, and after comparison of data, the conclusion was made that segmented 2D riblets are unlikely to outperform continuous 2D riblets



(a)



(b)

Figure 8. Comparison of drag reduction over optimum continuous blade riblets with optimum segmented trapezoidal blade riblets. (a) Segmented riblets were staggered as shown. Spacing between offset rows is  $s/2$ , while spacing between corresponding rows is  $s$ . (b) Optimal  $h/s$  ratio for staggered blade riblets is 0.4. Staggered blade riblets provide less drag reduction benefit than continuous blade riblets. All experiments performed using oil as the test fluid (Adapted from Bechert, et al., 1997b, 2000a).

In the true 3D realm, it has been theorized for some time that scales on which shark skin riblets are commonly grouped contribute to the performance of some shark skin varieties. By creating a pressure-exchange system below the scale surface, it was theorized that injection methods may have a pressure streak cancellation effect in the viscous sublayer, but concluded that the increased momentum exchange created would

have deleterious effects (Wilkinson, 1983; Bechert and Hoppe, 1985; Bechert et al., 1986). More recently there have been studies which have investigated the drag reduction properties of riblet-topped shark scales as both a static structure (Jung and Bhushan, 2010) and a flexible—possibly controllable—member (Lang et al., 2008). Using the scales molded in epoxy resin from the skin of the Spiny Dogfish (*Squalus acanthias*), shown in figure 9a, Jung and Bhushan (2010) have achieved a decrease in pressure drop versus a smooth surface in a rectangular flow cell flow experiment (Fig. 10a).

Additionally, a minimal decrease in pressure drop was realized in a similar experiment using segmented aligned riblets fabricated on acrylic (Fig. 9b) compared to a smooth acrylic test section (Fig. 10b). Certain sharks are known to exhibit riblet-topped scales that are attached somewhat flexibly to the underlying surface of the shark skin. These scales are able to change their pitch angle by bristling. As the pressure beneath the scale attachments changes, the flexible member changes position, and the trailing edge of the scales can lift up. Alternatively, the scales may bristle at concave skin locations that occur during the natural swimming. In an experiment simulating the bristling of flexible riblet covered scales into the boundary layer as a possible mechanism of control and drag reduction, no drag reduction benefit was achieved through extreme scale bristling. However, notable flow phenomena were found to occur as a result of scale bristling, including the formation of three distinct vortex shapes (Lang et al., 2008).

### *2.3.3 Riblet trends in pipe flow*

Riblet effects in pipe flow have been studied as well, and general patterns exist in the drag reduction benefit of sawtooth riblets. Due to the difficulty of riblet application

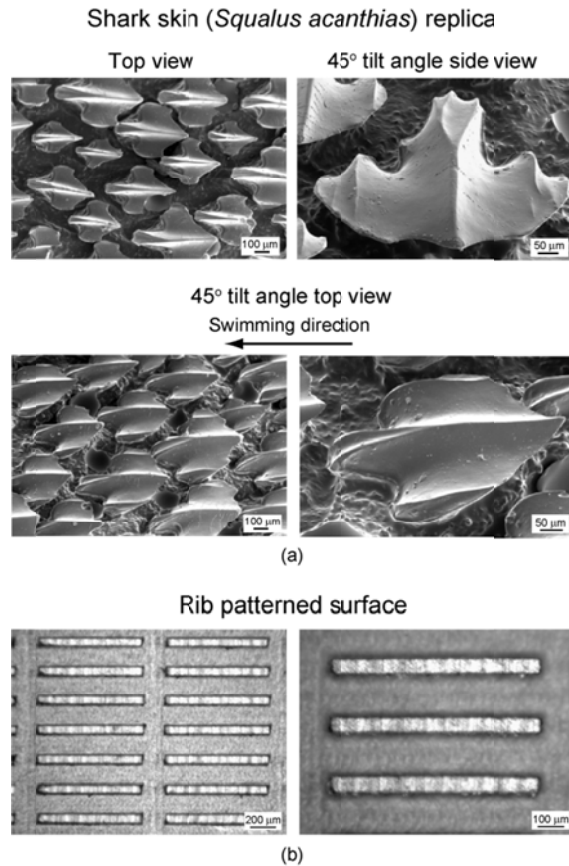
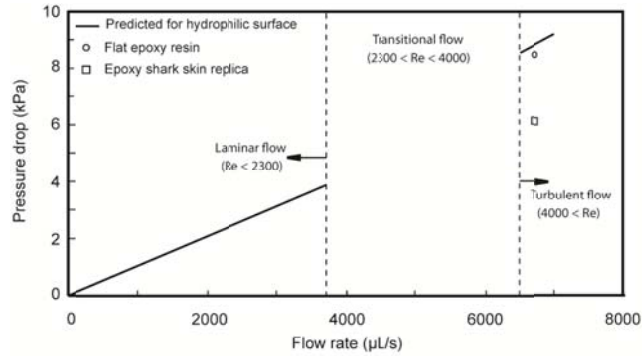


Figure 9. (a) SEM micrographs of shark skin replica patterned in epoxy. (b) Segmented bade-style riblets fabricated from acrylic. (Jung and Bhushan, 2010).

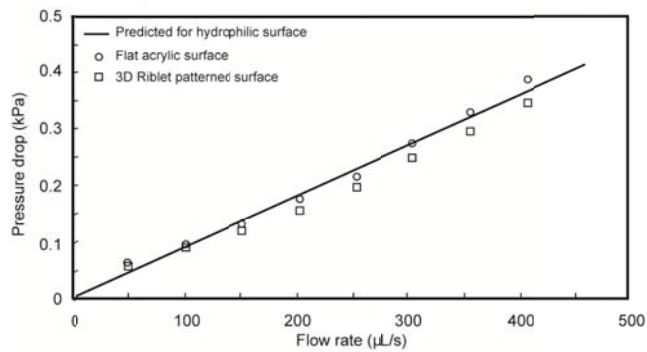
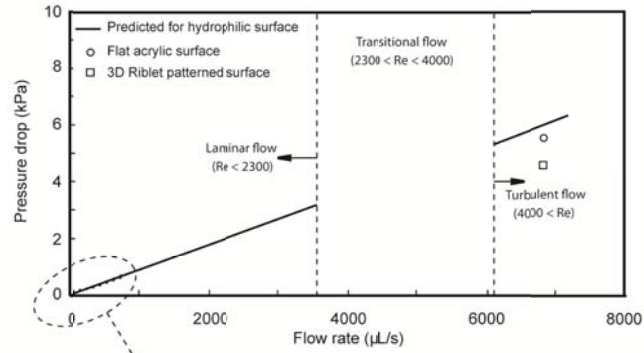
in pipes, data is generally limited to applications of sawtooth riblet film produced by 3M (Liu et al., 1990; Rohr et al., 1992). Drag reduction tests in pipe flow are carried out by comparing the pressure drop in a riblet-lined pipe with that of a similar smooth pipe.

Drag reduction data for sawtooth riblets on a flat plate are shown in figure 11a, and drag reduction data for water flow in sawtooth riblet lined pipes are shown in figure 11b. As riblets are applied to the inside surface of a pipe, the riblet tips are shifted together due to the curve of the pipe wall. Consequently, the optimized  $s^+$  range for riblets in pipe flow is lower than that for the same riblets in flow over a flat

surface (Liu et al., 1990). Additionally, the decrease in  $s^+$  suggests that an increased drag reduction in round pipes might be seen with a larger characteristic angle,  $\alpha$ , than for flow over riblets on a flat surface.



(a)



(b)

Figure 10. (a) Comparison of pressure drop in rectangular pipe flow over flat epoxy surface with shark skin replica surface. (b) Comparison of pressure drop in rectangular pipe flow over flat acrylic surface and segmented blade riblets. Data are compared with the predicted pressure drop function for a hydrophilic surface. All experiments performed using water as the test fluid (adapted from Jung and Bhushan, 2010).

## **2.4 Riblet fabrication and applications**

Riblet manufacture for study and large-scale applications has been one of the main difficulties in the field. Typical microscale manufacturing techniques are ill-fitted for large scale application due to the associated costs. Even for study, most researchers have opted for traditional milling or molding methods over the microfabrication techniques used in the microtechnology industry. Though non-dimensional units allow for comparison between flow fields of different fluids and at different conditions, the accurate microscale manufacture of riblets for experimentation has been a field of study in its own right. The largest difficulty in optimizing riblet geometries has been the fabrication of riblet series with incremental changes in characteristic dimension. Riblets used in airflow require spacings at or below 1 mm due to the low viscosity of air and the high speed at which wind tunnels must operate to create accurately measurable shear stresses on a test surface. Conversely, studies in an oil channel are carried out in flow that is both highly viscous and slower moving. This allows for riblets to be made with spacings in the 3-10 mm range (Bechert et al., 1992).

Commercial and experimental application of riblets outside wind tunnels and test stands is also limited by the high costs for less-than-optimal riblet performance. Application of riblets on a large scale has been done for several studies as well as for competition and retail purposes. Sawtooth riblets on vinyl films produced by 3M riblets have been applied on surfaces ranging from boat hulls to airplanes. Racing swimsuits produced by Speedo and others also employ a riblet pattern on the surface to reduce drag

during the streamline portion of each lap of a race (Krieger, 2004). Additionally, a novel surface scratching technique has been applied to the inside surface of pipelines to create a faux-riblet surface (Weiss, 1997).

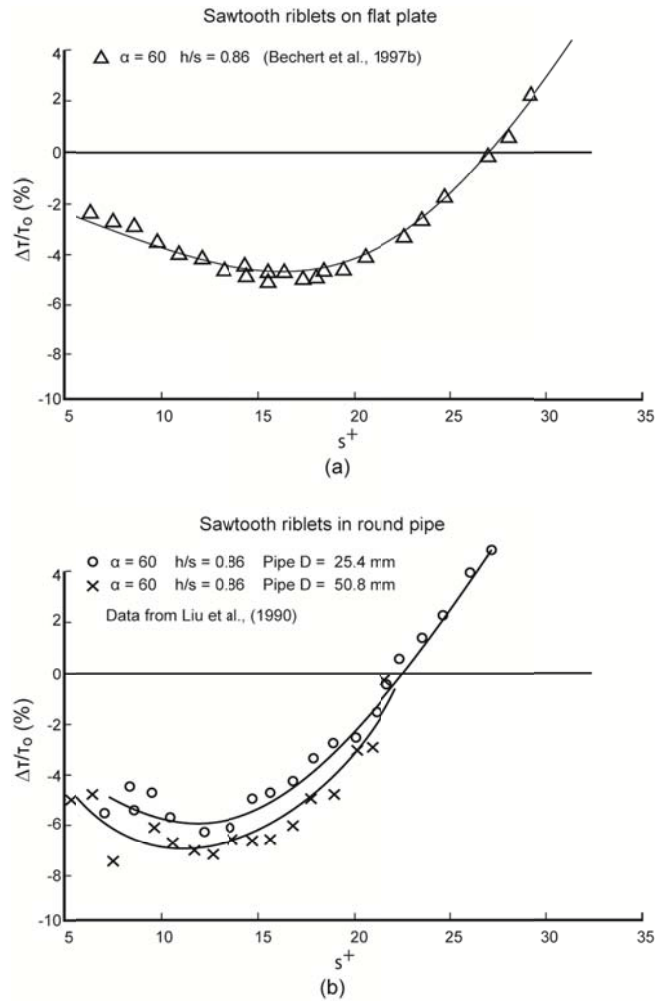


Figure 11. Comparison of riblet performance curves over sawtooth riblets on a flat-plate surface and inside round pipes of 25.4 mm and 50.8 mm diameters. Peak drag reduction for riblets in pipe flow occurs near  $s^+ = 12$ , which is lower than the flat plate optimal value of  $s^+ = 15$ . Bechert experiments performed using oil as the test fluid, and Liu experiments performed using water as the test fluid (adapted from Liu, et al., 1990; Bechert et al., 1997b).

### 2.4.1. Riblet dimension selection

Though the turbulent flow regime is characterized by completely random flow, the thickness of the viscous sublayer and the width of the streamwise vortices—and therefore the optimal riblet spacing—is dependent on properties of the fluid flow. Riblet spacing is the basis of other riblet dimensions, so the calculation of proper spacing is critical in riblet design. To calculate riblet spacing, wall shear stress must be known. Approximation of wall shear stress in rectangular channels can be done by combining Blasius' law for the friction coefficient with the Fanning friction factor and solving for wall shear stress. Blasius' law for friction coefficient is defined as  $c_f = 0.0791(Vd/\nu)^{-1/4}$ , where  $\nu$  is the kinematic viscosity and  $d = 4A/p$  is the hydraulic diameter of the channel where  $A$  is the cross sectional area and  $p$  is the wetted perimeter. The Fanning friction factor is a dimensionless number defined as  $c_f = 2\tau_0/\rho V^2$ , where  $\tau_0$  is the wall shear stress,  $\rho$  is the fluid density, and  $V$  is the average flow velocity. Combining equations, wall shear stress can be approximated by  $\tau_0 = 0.03955\nu^{1/4}\rho V^{7/4}d^{-1/4}$ .

Using the optimization comparison data in figure 6a, we know that a non-dimensionalized spacing should be chosen in the range  $15 < s^+ < 18$ . To calculate physical spacing,  $s$ , from  $s^+$ , the non-dimensionalization factor is used such that  $s = s^+ \nu / V_t$ , where  $V_t = (\tau_0/\rho)^{0.5}$  is the wall stress velocity. Using the optimization curves for each riblet shape in figure 5, the optimal spacing-based characteristic dimensions can be used to solve for optimal physical riblet dimensions.

#### *2.4.2. Application of riblets for drag reduction*

The transition between research and application of technologies is often slow, and riblet surfaces have been no different. Because of the limitations of past riblet technologies, both benefit in commercial applications and the methods of application have been limited. Because riblets provide drag reduction on objects where the dominant form of drag is caused by turbulent flow at the surface, only objects of a certain form factor will show any measurable benefit. A large portion of the total drag on long objects with relatively flat sides usually comes from turbulence at the wall, so riblets will have an appreciable effect. However, for objects like automobiles, where pressure drag or flow separation is the dominant form of drag, application of riblets would have minimal effect.

Beginning in the mid-1980s, vinyl film sawtooth riblets have been applied to boat hulls for racing. Both an Olympic rowing boat and an Americas Cup sailing yacht have been covered with riblets during competition. Because skin friction of an airplane accounts for as much as 48% of total drag, vinyl film riblets have also been applied to test planes of both Boeing and Airbus. These films haven't seen use on standard commercial flights yet, but the benefits seen in testing should not go unmentioned. Application of riblets to an airplane requires that several concessions are made. Several locations that would be covered by riblets must be left uncovered due to environmental factors; windows are not covered for the sake of visibility, several locations where dust and debris contacts the airplane during flight are left bare because the riblets would be eroded during flight, and locations where deicing, fuel, or hydraulic fluid would come in contact with the riblets are left bare. After these concessions, the riblets covering the remaining

70% of the aircraft have provided 3% total drag reduction. This 3% drag reduction correlates to a similar 3% savings in fuel costs (Bechert et al., 1997a).

Another large commercial application for riblet technologies is drag reduction in pipe flow. Machining the surface or applying vinyl film riblets proves difficult in the confines of most pipes, and an alternate solution must be used. Experimental application of a scratching technique to the inside surface of pipes has created a riblet-like roughness that has provided more than 5% drag reduction benefit (Weiss, 1997). Stemming from an old sailors' belief that ships sail faster when their hulls are sanded in the longitudinal direction, Weiss fabricated these riblets by using a steel brush moved through the pipeline to create a ridged surface. Studies have shown as much as a 10% reduction in fluid flow with the combined effect of cleaning the pipe and ridging the surface. Tests on a 10 mile gas pipeline section have confirmed this benefit during commercial operation (Bechert et al., 1997a).

The dominant and perhaps only commercial market where riblet technology for drag reduction is commercially sold is competitive swimwear. The general population became aware of shark skin's drag reduction benefits with the introduction of the FastSkin® suits by Speedo in 2004. Speedo claimed a drag reduction of several percent in a static test compared to other race suits. However, given the compromises of riblet geometry made during manufacturing, it is hard to believe the full extent of the drag reduction.

It is clear that creating surface structures by weaving threads is difficult. As a result, riblet geometries woven from thread have limited options of feasible riblet shapes.

By the pattern woven into the FastSkin® swimsuits, riblets are formed which resemble wide blade riblets with small grooves on top. The larger riblets are formed by the macro weaving pattern, and the smaller riblets are created by the individual weaves of thread aligned with the macro riblets. Both of these riblet-like shapes are distinguishable in figure 12. As shown in figure 12a, unstretched riblets are tightly packed. As the fabric

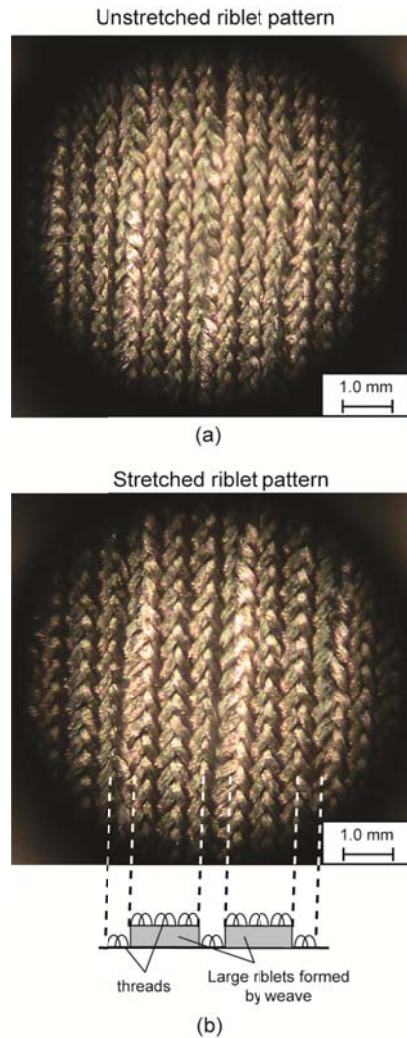


Figure 12. Images of riblet geometries on (a) unstretched and (b) stretched Speedo FastSkin® swimsuit. (c) Schematic showing apparent hierarchical riblet structure formed by threads.

stretches, the riblet width and spacing increase. The associated decrease in  $h/s$  ratio depends on the dimensions of each swimmer's body, which is another compromising factor in the design. Riblet thickness is also a factor considered in the design. Aside from the limitations imposed by the weaving patterns available, flexibility in the riblet tips will hinder the fabric's ability to impede the cross-stream translation of streamwise vortices. Thicker riblets are needed likely used for strength, and cause a decrease in the peak drag reduction capability compared to thinner riblets.

#### *2.4.3 Riblet fabrication methods for study and applications*

For experimentation, many riblet geometries have been made through careful machining of riblets from stock, but standard machining techniques lack the precision required to make riblets for use in high speed air flow. Additionally, machining lacks the flexibility to fabricate small-scale riblets with enough resolution to create incrementally different samples for true optimization of sawtooth and scalloped riblets. Using a small-scale computer numerically controlled (CNC) mill, segmented blade riblets have been fabricated in acrylic with a thickness of only 38  $\mu\text{m}$  and a height of 90  $\mu\text{m}$  (Jung and Bhushan, 2010). Scalloped and sawtooth riblets have been machined in aluminum at spacings in the sub-millimeter range (Walsh and Lindemann, 1984).

Another method used to construct blade riblets is to assemble separately fabricated parts. By fabricating thin element blades and spacers, stacked-assemblies with adjustable geometry were created (Bechert et al., 1997b). By manufacturing blades in this separate manner, thinner blades can be fabricated using rolling techniques that eliminate the concern of milling errors ruining test plates. Riblet spacing is controlled by

the added tolerances of each blade and spacer, which allows for an increase in overall fabrication tolerance. The major advantages of this method of assembly are ease of adjustment and less danger of milling errors destroying test plates. Optical images of these assembled riblets can be seen in figure 8a

For scale replicas and 3D riblets, the complex shapes required usually afford molding as the fabrication method. Micro-molding and micro-embossing has been evaluated using polymethyl methacrylate (PMMA) as the mold material and a silicone rubber as the replica material (Xin and Zhang, 2008). Replicas were shown to lack resolution by 2.2% and 5.5% of the groove spacing and 8.3% and 5.9% of the height, respectively. Alternatively, epoxy replicas of shark skin have been molded in dental wax reliefs taken from shark skin and studied in flow cell experiments in a rectangular pipe section (Jung and Bhushan, 2010). SEM images of these replicas can be seen in figure 9a.

Many of these fabrication methods are not suitable for use outside laboratory settings. The wear experienced in a physical environment where riblets would provide measurable drag benefits would quickly render many of the above models non-beneficial. Additionally, fabrication for application on large-scale is a concern with most of these methods. Other methods of riblet manufacturing have been studied for use in production environments. 3M vinyl film riblets have been used in myriad riblet performance studies, and the fabrication of riblets by microprofile grinding and incremental rolling processes have been investigated.

3M vinyl film riblets (Marentic and Morris, 1992) have been applied to many test surfaces, including the inside of various pipes for pipe flow studies (Koury and Virk, 1995), flat plates in flow channels and wind tunnels, boat hulls in towing tanks (Choi et al., 1989), airplane wings (Han, 2002), and airplane fuselages. Similar riblet films have been fabricated using bulk micromachining of silicon to create a master for molding of Polydimethylsiloxane (PDMS) to create a thin, flexible riblet film. This film has been used in flow visualization tests (Lee and Choi, 2008)

Grinding and rolling methods of riblet fabrication have been studied for application in both research and large-scale application. A profiled grinding wheel has been used to fabricate several riblet geometries based on sawtooth riblets with  $h = 20 \mu\text{m}$  and  $s = 50 \mu\text{m}$  (Denkena et al., 2008). Dressing of the grinding wheel was done with diamond-profile roller used in a two-step process in which the profile roller dresses every second tooth on the first pass, shifts axially the distance of one riblet spacing, and dresses the remaining teeth on a second pass. One downside of the grinding process is the lack of hardening on the final riblet surface. Alternatively, rolling methods can be used to strain harden the riblets during fabrication. Using a roller with the profile of two-riblets on its outer face, a linearly patterned rolling process has been used to fabricate scalloped riblets in a titanium alloy with  $h = 162 \mu\text{m}$  and  $s = 340 \mu\text{m}$  (Klocke et al., 2007). The strain hardening, favorable grain patterns, and residual compressive stresses in the riblet surface after fabrication provide advantages in riblet strength for production applications.

## **2.5. Effect of slip length and polymer additives on fluid drag**

Surfaces form molecular bonds with fluid molecules traveling across them. This attraction is not the same for all surface-fluid pairs, due to the different interactions between molecule pairings. For this reason, classical non-dimensionalization of these riblet tests is limited in applicability to fluid-surface pairings which can be approximated to have zero slip length. Non-dimensionalized data presentation does not allow for perfect comparison between studies done with different surface materials or fluids. Figure 13 shows a comparison between riblet performance measured in external flow using air and oil as fluids. It is clear that a similar behavior is exhibited by both riblet studies, but the data sets do not match. The interactions between fluid molecules and the surface material, in addition to measurement resolution and accuracy cause the experimental data to vary greatly throughout the range of  $s^+$ .

Another factor important to the drag experienced in fluid flow is the presence of polymer additives to the flow. The interaction between polymeric agents and the molecules of fluid in turbulent flow causes a large reduction in drag to occur. Fish are known to secrete an amount of mucus as they swim, which reduces the drag experienced effects on the fish. Though sharks do not secrete enough mucus to use this mechanism for drag reduction, small amounts of mucus are present on the skin of sharks (Bechert et al., 1986).

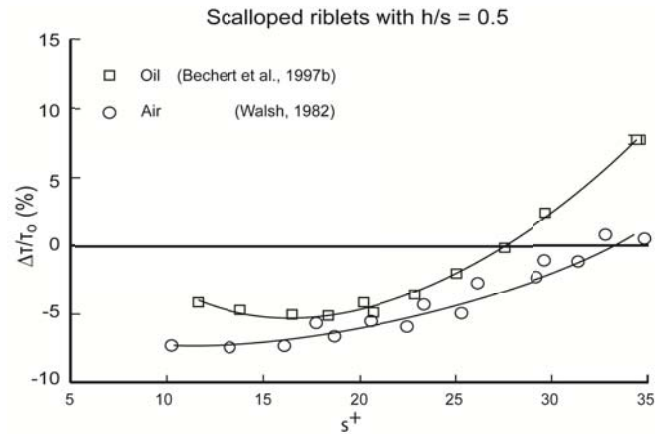


Figure 13 Comparison of drag reduction with oil and air on similar sawtooth surfaces (adapted from Walsh, 1982; Bechert et al., 1997b)

### 2.5.1 The effect of fluid-surface bonding on drag reduction

The degree to which bonding occurs between fluid molecules and the surface on which they rest can be described in many ways. For a small droplet placed on a surface, the contact angle is the angle formed between the surface and the tangent line of a droplet where it contacts the surface. A perfect sphere of fluid on a surface has a contact angle of  $180^\circ$ , and a film of water has a contact angle of  $0^\circ$ . Another method of surface-fluid bonding characterization is the roll-off angle. This is the angle at which a drop of fluid previously at rest on a horizontal surface will move across a surface. Fluid molecules with a low affinity for intra-species bonding and a higher affinity for fluid-surface bonding will have a low contact angle and a high roll-off angle. Fluids which have higher strength inter-species bonds than fluid-surface bonds will have high contact angle and low roll off angle. Two common fluids whose surface attraction properties are studied are water and oil. A surface which forms a contact angle with water less than  $90^\circ$

is said to be hydrophilic (water loving). If the same interface has a contact angle greater than  $90^\circ$ , it is said to be hydrophobic (water fearing). Surfaces with a contact angle greater than  $150^\circ$  are said to be superhydrophobic. To achieve superhydrophobicity, surface roughness must be applied in addition to typical material coatings. Surfaces which have the same contact angle regimes when exposed to oil are said to be oleophilic, oleophobic, or superoleophobic.

An obvious but often overlooked consequence of these fluid-surface interactions is fluid drag. Where in classical fluid dynamics, a no-slip condition is assumed at the interaction between a fluid and a surface, fluids which have high contact angle and low roll off angle measurements may exhibit a small slip length at the surface. Figure 14 shows a comparison of the velocity profile of a hydrophilic surface with a no-slip condition to the velocity profile of a hydrophobic surface with slip at the surface. The distance by which the apparent flow origin is below the surface is called the slip length. The increase in velocity near the surface translates to a corresponding increase in

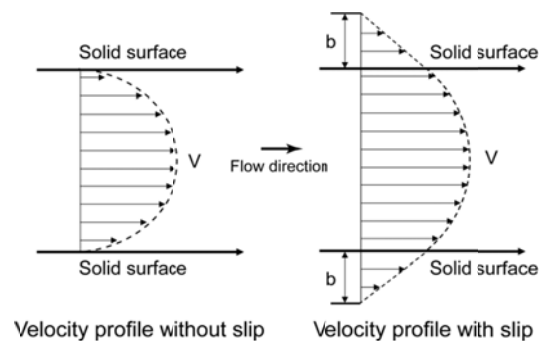


Figure 14 Schematic of velocity profiles with and without boundary slip. Slip length,  $b$ , occurs on hydrophobic surfaces (Jung and Bhushan, 2010)

maximum flow velocity and a decrease in drag. Pipes coated in low surface energy materials exhibit a decrease in pressure drop compared with similar pipes which have higher surface energy coatings. Figure 15 shows laminar and turbulent pressure drop comparisons for a flow-cell experiment in which hydrophilic, hydrophobic, and superhydrophobic surfaces in water flow. The greatest decrease in pressure drop and fluid drag happens for the superhydrophobic surface (Ou et al., 2004; Jung and Bhushan, 2010). This behavior is similar for interactions between other fluid-surface pairs. Reducing the strength of bonding between the fluid molecules and the surface causes a corresponding reduction in fluid drag in both the laminar and turbulent regimes.

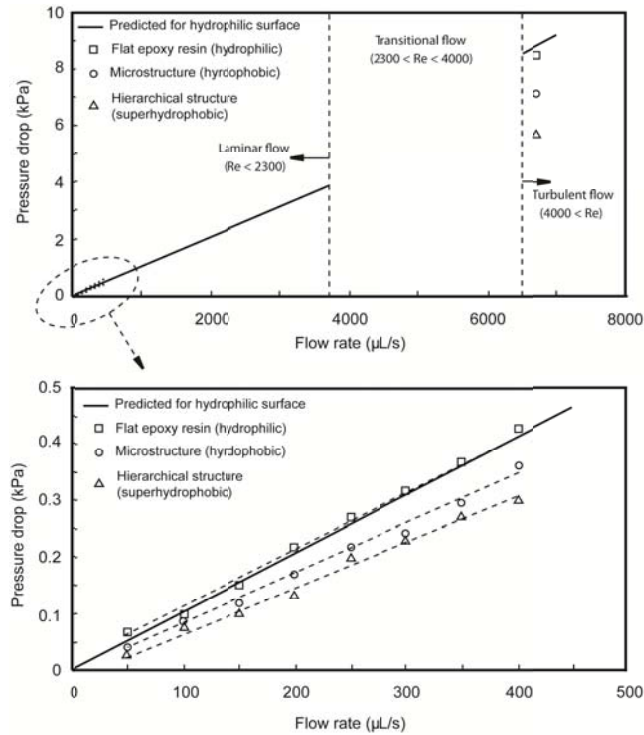


Figure 15 Comparison of pressure drop in pipe flow of hydrophilic, hydrophobic, and superhydrophobic surfaces in laminar and turbulent flow regimes. Decreased pressure drop in pipe flow corresponds to decreased drag (adapted from Jung and Bhushan, 2010)

### 2.5.2. *Effect of fish mucus and polymers on fluid drag*

Fish are known to secrete mucus during swimming. Though it is not known whether the mucus is present at all times, it is known that certain environmental factors cause, alter, or enhance the production of mucus. These environmental stressors may present a need for increased swimming speed to catch or avoid becoming prey, protect against non-predatory threats such as micro-organisms, or resist abrasion while swimming near rocky surfaces. Regardless of which events cause fish to secrete mucus, the drag reduction benefits of mucus are known. Numerous experiments have demonstrated the drag reduction possible with mucus covered fish-shapes compared to non-mucus covered fish-shapes (Hoyt, 1975). In an experiment comparing the drag on wax models to a mucus covered fish, a reduction in skin friction drag of 50% was seen (Daniel, 1981).

Similar to these fish mucus experiments, polymer additives in pipe flows have been known for many years to reduce the drag in fluid flows by extreme amounts. In a pipe flow study comparing various injection techniques of polymer solutions into water, drag reductions of up to 80% were achieved (Frings, 1988). Additionally, the drag reduction benefit increases with increased Reynolds number. While this works well for pipe flows, in which the polymer remains mixed and active throughout the length of the pipe, its application to external flows is much more difficult. Mucus on fish does not mix well with water in static contact, but does mix and provide drag reduction during dynamic contact. By this feature, the mucus use of fish is minimized. Unfortunately for any long range application of polymer drag reduction on an external flow, the polymer

solution must be continuously injected. This would cause large quantities of the solution to be used and likely render the strategy inefficient in terms of overall energy use.

Though sharks do not secrete enough mucus to use this mechanism for drag reduction, small amounts of mucus are present on the skin of sharks (Bechert et al., 1986). It is possible that shark skin mucus secretion is similar to fish, where only environmental stressors or swimming causes an increase in output, but the total quantity of mucus on the surface at any given time is low. One possible mechanism by which this trace quantity of mucus could be useful is in changing the flow characteristics in only the riblet valleys—where lower speed flow covers a large surface area—or at only the riblet peaks—where shear stresses are highest. These small effects near the surface may propagate into a larger benefit as the lines of constant velocity in the flow shift and condense as shown speculatively in figure 16. The localized effect of mucus secretion in the valleys or at the peaks would be similar to the effects of a partially hydrophobic surface. By coating a riblet surface with a hydrophobic layer in the valleys (Fig. 16b), at the peaks, and as a whole, comparisons can be drawn between the drag reduction effects of trace amounts of mucus found on shark skin.

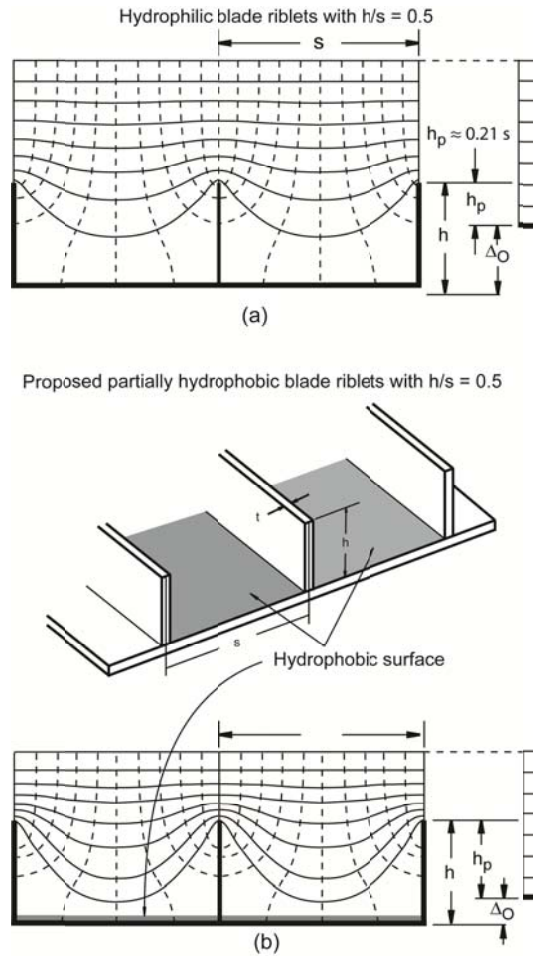


Figure 16 (a) Behavior of hydrophilic surface in fluid flow. (b) Proposed deposition of hydrophobic surface on portions of blade riblet surface should increase the protrusion height of riblets and increase drag reduction benefit

## 2.6 Summary and Outlook

Fluid drag in the turbulent boundary layer is in large part due to the effects of the streamwise vortices formed in the fluid closest to the surface. Turbulence and associated momentum transfer in the outer boundary layers is in large part due to the translation, ejection, and twisting of these vortices. Additionally, the vortices also cause high local velocities at the surface which create large shear stresses on the surface. Riblets reduce drag by two mechanisms. First, by impeding the translation of the streamwise vortices, ejection and outer layer turbulence is reduced. Second, by lifting the vortices from the surface and reducing the area exposed to the high velocity flow, riblets facilitate a net reduction in shear stress at the surface.

Various riblet shapes have been studied for their drag reducing capabilities, but sawtooth, scalloped, and blade riblets are most common. By varying flow properties or riblet geometries, optimization studies have been performed. Drag reduction by riblet surfaces has been shown to be as high as nearly 10% given an optimal geometry of  $h/s \sim 0.5$  for blade riblets with a no-slip condition. The maximum reliable drag reduction provided by scalloped riblets and sawtooth riblets is about 6% at  $h/s \sim 0.7$  and 5% at  $\alpha \sim 60^\circ$ , respectively. Experimentation of other shapes has provided similar benefits of around 5% drag reduction. Additional experimentation with simple 3D shapes, such as offset segmented blade riblets, has shown comparable performance to standard blade riblets, but hierarchical structures and complex 3D shapes have yet to show improved benefit. The behavior of static and dynamic versions of complex 3D replicas has been minimally investigated, and much work remains in understanding the complexities that

are involved. To date, no improved drag reduction has been accomplished using replica models, but hypothesized control mechanisms for dynamic replicas have been proposed. Though the optimum shape for drag reduction performance is blade riblets, the fragile nature of these blades makes their commercial application of little use. Scalloped and sawtooth riblets, which provide considerably less drag reduction benefit, are much stronger shapes mechanically speaking and should be used for application in environments where contact may occur with non-fluid materials.

Commercial applications of riblets include competition swimsuits, which use a thread-based riblet geometry, as well as experimental applications to airplanes. Drag reductions in riblet application have been accomplished, and flight applications have seen a fuel savings of as much as three percent. Manufacturing techniques for riblets must also be chosen specific to their application. Vinyl film riblets are the easiest method, as application of a film to a surface requires less for work small scale application than other methods. Rolling or grinding methods of riblet application should be investigated for turbine blades or high volume commercially sold pieces. Machining methods are unfavorable in most instances, and should be avoided in most instances of non-research riblet application.

There are many front of riblet research which must be investigated further. Static and dynamic riblet-topped scales, as well as partially-to-fully hydrophobic riblet surfaces must be investigated. Additionally, further investigation is needed into internal flow riblet applications, as all internal-flow riblet studies to date have been performed on

round pipe. Understanding the effects of riblets in rectangular duct flow was the primary objective of this thesis.

## CHAPTER 3

### THE EFFECTS OF SHARK SKIN INSPIRED RIBLET GEOMETRIES IN INTERNAL RECTANGULAR DUCT FLOW

#### 3.1 Experimental Design

##### 3.1.1 Test Setup Design

A flow cell was designed for use in water which features interchangeable test sections. A non-scale diagram of the test setup, including the flow cell, pump, measurement devices and the control valves, is shown in figure 17. A pump recirculates water through two parallel loops; The Test Loop, which consists of the test section, measurement devices, and the control valve, and the Bypass Loop, which consists of a resistance valve and a path which bypasses the flow cell and meets the return path to the inlet of the pump. By increasing or decreasing the overall resistance of the Test Loop, the control valve increases or decreases the flow rate through the test section. Including a return loop causes a small decrease in the maximum flow rate achievable in the Test Loop, but is needed to ensure that pump does not heat the water by spinning when the Test Loop is reduced to very low flow rates. The resistance valve on the Bypass Loop allows the resistance in the Return Loop to be selected by the operator. For the purposes of these experiments, this resistance was selected such that with the control valve open, flow rates high enough to achieve turbulent flow were achievable, but with the control

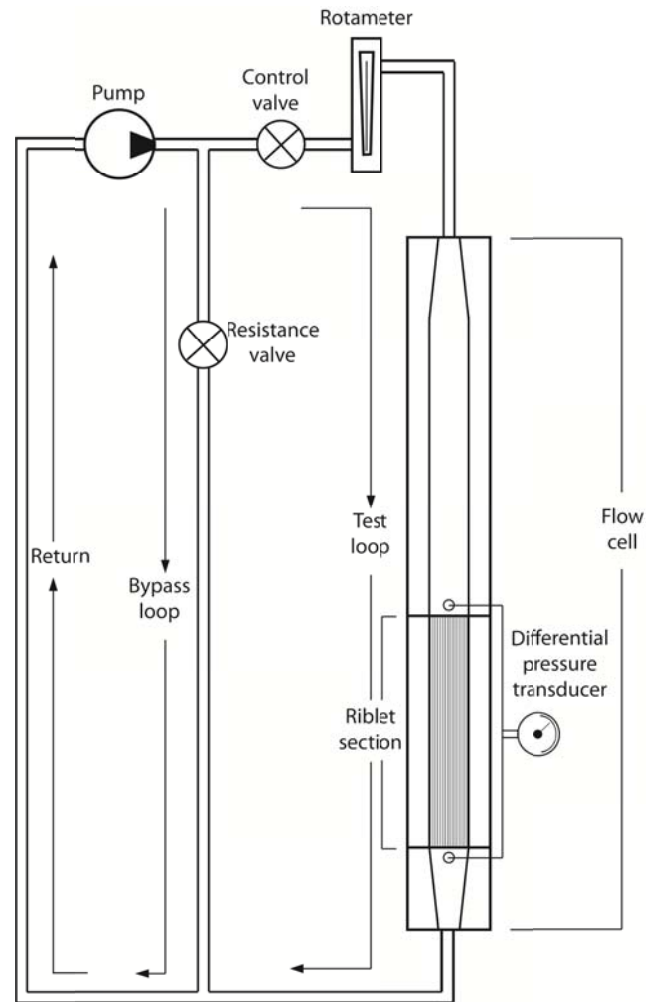


Figure 17. Schematic representation of experimental setup showing the pump, test loop, bypass loop, and return. The test loop consists of a control valve for varying flow velocity, a rotameter for measuring flow rate, a differential pressure transducer, and the flow cell with the riblet test section shown. The bypass loop consists of only a resistance valve, which is used prior to all experimentation to adjust the flow rate limits of the system within the pumps working pressure range.

valve fully closed, the pump was still able to generate high flow rates and avoid heating the water. Additional equipment which was used for in the test setup includes a TEEL 4RH55 centrifugal pump, an Omega PX26-005DV Differential Transducer, a Vishay 2311 Laboratory Amplifier, a Measurement Computing USB-1208LS DAQ card, and

two rotameters with overlapping ranges from 1Lpm to 40Lpm. Tap water was used for this experiment, and was maintained between 23°C and 25°C for all experiments. Calculations were performed with water viscosity calculated for this temperature to ensure accuracy.

The flow cell was designed within many constraints, including those of fluid dynamics, fabrication, assembly, reusability, and cost. Acrylic was used for fabrication of all sections of the flow cell, selected for its strength and transparency in addition to its ability to be easily and precisely milled. The flow cell, which is approximately 1m in overall length from inlet to outlet, is constructed of three layers of acrylic, with the duct forming between the topmost and bottommost layers, bounded on each side separate pieces of acrylic which were precisely milled to the correct height of the channel. A test section 25.4 cm long was built after a 45 cm section, which allows the flow to develop, and followed by a shorter section, which allows the flow to be collected at the outlet with minimal effects from the end of the channel. Additionally, spacers can be added or removed from each side of the channel to adjust its width to either 3 cm or 4 cm. This adjustability in size allows for multiple experiments to be run in the same flow cell, saving time and cost while gathering data and comparing findings in multiple duct arrangements. On either end of the test section, a hold was milled and threaded for pressure measurement. Care was taken to mill these holes precisely and to maintain equivalent sharp edges on both hold locations for the purpose of avoiding measurement error.

Assembly of the flow cell was performed in several phases. The first phase involved assembling all components of the flow cell with the exception of the top and bottom of the test section. Each section was coated with a thin layer of Silicone sealant and set in place carefully. Care was taken to avoid allowing any of the sealant to intrude into the internal cavity which the water would flow through. After all components were set in place, bolts were inserted into holes which aligned each layer of the flow cell. Bolts were tightened and the flow cell was allowed to sit overnight to provide ample time for drying of the sealant. The second phase of the assembly included carefully and precisely drilling and tapping holes for  $\frac{1}{2}$  in NPT pipe threads, which were used for inlet and outlet fittings. The precise alignment of each layer of the flow cell is required to ensure the alignment of the threads upon disassembly and reassembly. After these holes were drilled and tapped, the fittings were threaded into place and sealed with a thin layer of silicone sealant. The third phase of the assembly included mounting the initial test surface to the flow cell in much the same way as the phase 1 assembly was performed. A thin layer of silicone sealant was applied to each mounting face of the test sections, and they were carefully placed and aligned. Care was again taken to ensure that no sealant protruded into the test section, and the bolts were then inserted and tightened down. Finally, the pressure tap fittings were inserted fully into the tapped holes before and after the test section. Tap fittings were chosen that, when fully inserted into the acrylic layer, would not impede the flow by protruding into the bulk flow. Transparent tubes were then pressed onto the fittings for connection to the differential pressure transducer after calibration.

A data acquisition system was designed to sample and store differential pressure data across the test section for the duration of the testing at each flow rate which was tested. The differential pressure transducer which was used had a range which exceeded the requirements of the system, but was suitable for use. A Vishay amplifier was used to power the transducer and amplify its output signal, which was then read by the USB DAQ and accompanying software. Samples were taken at a rate of 10 Hz for a duration of 1 minute for each flow rate which was tested. This provided an available 600 data points from which an average was taken.

### *3.1.2 Calibration and System Operation*

The DAQ system was calibrated prior to use with an Ametek RK-1600W6 pneumatic pressure tester. The amplifier was first turned on and let come to its steady state operating temperature overnight, and then the DAQ system was calibrated with the downstream end of the differential pressure transducer was open to atmospheric pressure, and the upstream side was increased incrementally above atmospheric pressure. Several calibration plots were taken to ensure stability of the system.

Prior to system operation, the flow cell required preparation for use to remove all air bubbles and protect the system from external influences. The pump inlet hose was disconnected from the system return fitting, and the separated components were placed in a reservoir full of clean water. Clamps were placed over the pressure tap tubes, and the pump was primed and turned on. The control valve was then opened fully to allow high-speed flow to remove all air from both loops of the system. Transparency of most system components allowed for easy purging of air bubbles. After all air was purged from the

test section of the channel, the pressure tap tubes were unclamped to purge the remaining air with a small amount of water, and then re-clamped to prevent additional air from being pulled into the system when the pump was shut off. The pump inlet hose was then connected to the system return fitting, and the pump was shut off. The pressure tap tubes were then connected to the differential pressure transducer, and clamps were removed, allowing the system to remain free of air and provide reliable pressure measurements.

Operation of the system followed strict protocol to ensure the least error was introduced into the system. Prior to turning the pump on, the amplifier was zeroed using the auto balancing feature. This ensured that when there was no fluid velocity and the differential pressure across the test section was zero, the outputs of the amplifier were also zero. After ensuring a reliable zero point on the amplifier, the pump was turned on and the system was brought to its maximum reading achievable which, for all test pieces, was 6.5 gpm (24 lpm). Due to the calibration of the rotameter, all flow rate measurements were taken in gpm and converted to SI during calculations. Beginning with the highest achievable flow rate and moving down by 0.5 gpm increments (1.89 l) to a minimum reading on the larger rotameter of 1.5 gpm (5.68 lpm), the differential pressure across the test section was recorded for 1 minute at each flow rate. After all data was collected, the system was drained and the rotameter was switched to the lower-range rotameter. The system was again primed and purged of air in the same manner as listed above, and data was collected within the range of the small rotameter, from 0.3 gpm (1.14 lpm) to 2.0 gpm (7.57 lpm) at 0.3 gpm intervals. This data collection process was repeated multiple times for each test section, and the final results were again averaged

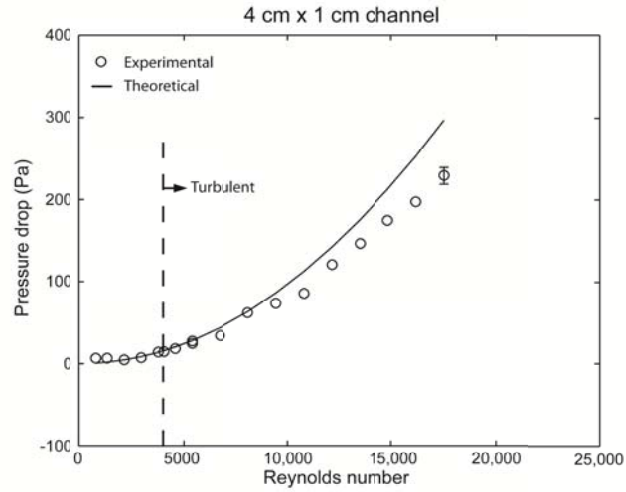
after inspection and comparison of trends. Error ranges of  $\pm 1$  standard deviation were calculated to be approximately 50 Pa for data sets from each test section. Calculations used all data points collected at the highest flowrate tested across the section.

The flow cell system was first tested with the flat plate test sections, and the resulting pressure drop curve was compared to the theoretical pressure drop for the test section of the pipe, which was calculated with the Darcy-Weisbach Equation

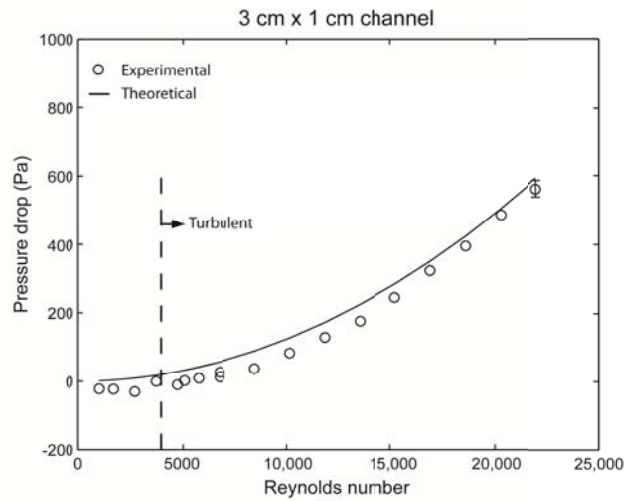
$$h_f = f \frac{LV^2}{2Dg} \quad (1)$$

where  $h_f$  is the pressure drop,  $f$  is the Darcy friction factor,  $L$  is the length of the test section,  $D$  is the hydraulic diameter of the pipe,  $V$  is the fluid velocity, and  $g$  is the gravitational constant. The Darcy friction factor was found using the Moody chart assuming a relative roughness of the Acrylic channel of 0.0001 and Reynolds values calculated from the hydraulic diameter of the duct. The actual and theoretical pressure drops were recorded and calculated for channels of both 3 cm and 4 cm widths. A strong correlation is evident between the actual pressure drop and the theoretical pressure drop (Fig. 18). With this confirmation that flow is behaving as theoretically expected, it was taken that flow was well developed through the test section.

Negative pressure drop readings at very low flow rates appear in the experimental data sets of the 3 cm channel. These negative values appear in all data sets on the 3 cm channel, including those taken later across riblet test section, and was attributed to a DC shift in the output of the amplifier.



(a)



(b)

Figure 18. (a) Pressure drop comparison between theoretical and experimental flat plate surfaces in a 4 cm x 1 cm channel demonstrating viability of the system. (b) Pressure drop comparison between theoretical and experimental flat plate surfaces in a 3 cm x 1 cm channel demonstrating viability of the system.

An additional consideration of the calibration and initial system flow measurements was to ensure that fully developed turbulent flow occurs across the test section. Since riblet effects are only beneficial in the turbulent regime, it was important to be certain of the system's turbulent nature. Duct flow turbulence and entrance length

can be calculated using the hydraulic diameter equation, standard Reynolds number equation, and turbulent entrance length equation. The hydraulic diameter of the system,

$$D_h = \frac{4BH}{(2B+2H)} \quad (2)$$

where B is the width of the channel and H is the height of the channel, is 1.68 cm for the 4 cm channel width and 1.57 cm for the 3 cm channel width. Using these values at each Reynolds number calculated using the various flow rates of the system, the entrance length of the system was calculated using the equation for turbulent entrance length,

$$le = 4.4D_h Re^{1/6} \quad (3)$$

is never greater than 38 cm in the 4 cm channel and 37 cm in the 3 cm channel. Given that the hydraulic diameter is most valid for rectangular ducts with aspect ratios near 1.0, concerns about the validity of the hydraulic diameter approximation led to investigations of the validity of the bounding conditions for this approximation. In channels where  $B \gg H$ , the hydraulic diameter can be approximates as twice the channel height. Using this approximation, the entrance lengths increase, but are never greater than 48 cm in the 4 cm channel and 50 cm in the 3 cm channel. The working assumption of this system is that the system behavior is valid at the hydraulic diameter approximation, but with a provided entrance length of 45 cm, there is a small margin of error allowed for more development room in the system.

### 3.1.3 Riblet Design

Riblets have been fabricated in myriad shapes, though most studies focus on three basic shapes which have been selected for reasons of fabrication and strength. Riblets have been primarily studied which have a 2-D cross section extruded in the direction of the flow. For the purposes of this study, which is meant to compare the effects of riblets in internal duct flow with the effects of riblets on external flat plate flow, this method was selected. This has both the benefit that there is a large body of data on external flow over 2-D riblets available for comparison and that fabrication methods exist which provide sufficient precision for the fabrication of the riblets. Riblets with a blade cross section were chosen for study due to their tendency to exhibit the highest drag reduction benefit of any currently studied riblet geometry.

From riblet studies summarized in a previous work, it is known that the maximum drag reduction of about 10% occurs for blade riblets which have an  $h/s$  ratio of 0.5, a thickness optimized for lowest width while still maintaining lateral strength, and an  $s^+$  value near 15 (Dean and Bhushan, 2010). This geometry was selected, and the size-selection process outlined in the above work was performed to determine physical riblet dimensions which would allow the riblets to operate in the turbulent regime while maintaining a usable range of  $s^+$  values. Several test-groupings of riblets were fabricated on individual test surfaces which featured riblets with dimensions sufficient for use in the turbulent regime throughout the expected optimal range of riblet benefit.

To cover a variety of riblet arrangements, two sets of riblet surface families were fabricated which allowed inspection and measurement of drag reduction effects of riblets

spanning a range of  $h/s$  ratios as well as a range of flow velocities and turbulence conditions. A sample riblet surface is shown in figure 19. The first set of riblets which was fabricated included blade riblets which have  $h/s$  ratios of 0.3, 0.5, and 0.7. Each set of riblets has an equal height—254  $\mu\text{m}$ — and similar thickness but varied spacing— 762  $\mu\text{m}$ , 508  $\mu\text{m}$ , and 356  $\mu\text{m}$ —ensuring similar protrusion into the flow for better comparison of riblet effects over the range of  $h/s$  ratios. The second set of riblets built upon the first set by manipulating the overall scale of the riblets with  $h/s$  ratio of 0.5 by incrementally decreasing both the height and spacing of the riblets to include spacings of 254  $\mu\text{m}$ , 356  $\mu\text{m}$ , and 508  $\mu\text{m}$  and corresponding heights. In this way, the  $s^+$  range of the riblets which is known to be beneficial in external flows was studied throughout the range of flow rates achievable by the channel. This size-adjustment allowed study of riblets from Reynolds numbers of 4000 to 20,000, and ensured that the majority of the turbulent range of the system was studied within the operational range of the riblets.

#### *3.1.4 Riblet Fabrication*

Fabrication of most macro components of the flow cell test setup was performed by a machine shop using mills of the proper size and accuracy to provide the required dimensional and flatness tolerances for leak-proof assembly of the flow cell with only thin layers of silicone adhesive, as described in the Experimental Design section above. Riblet test section blanks were fabricated in-house on a traditional Bridgeport knee mill by cutting the bulk shape of the test piece from a single piece of stock. Riblets were milled into the blank such that the riblets protruded up from the flat-plate surface and into

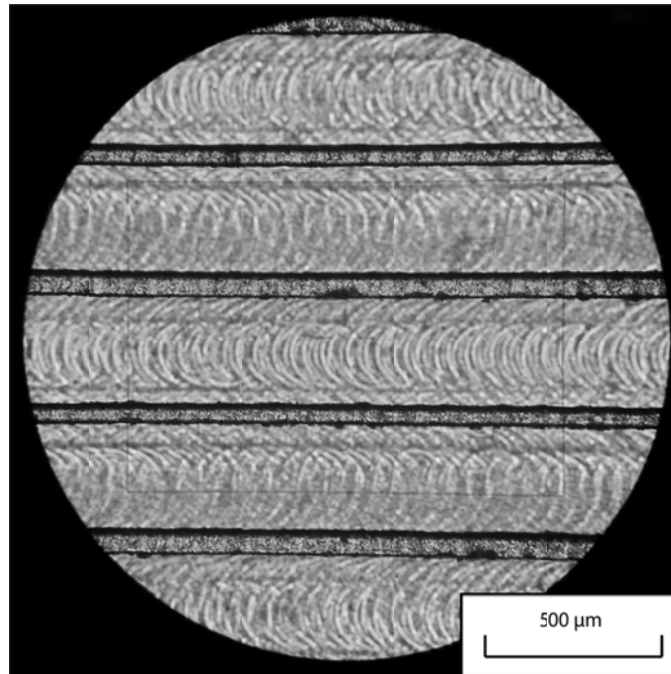


Figure 19. Microscope visualization of milled riblet surface. Dark lines are raised blade riblets, and lighter areas with swirl marks are milled valleys. Some amount of roughness is evident at the corners of each riblet peak as well as in the riblet valleys.

the flow. It is an important consideration that the riblets were fabricated to protrude into the flow when compared to the flat plate and not cut below the flat plate surface. The flat plate test surface was milled as a test section blank. Material left for riblets was milled off with a fly cutter. It is important to note that equal surface roughness is not guaranteed between the flat plate and riblet surfaces.

Milling of the riblets was performed using small-scale CNC mills which were adjusted for optimal precision and accuracy of milling. Tolerance of  $\pm 0.001$  in ( $25 \mu\text{m}$ ) was achievable on the smallest features. One drawback to the use of the small-scale mills is the lack of proper range of motion in the longitudinal, and as a result the riblet surfaces were milled in two passes with the test piece moved between passes. The process,

detailed below, is the outcome of many attempts at fabrication, the result of which is a reliable method for fabrication of riblet surfaces. Generally, the method of fabrication follows the following process: CNC code generation, mill adjustment, sacrificial test-piece setup and milling, production test-blank setup and milling, cleaning.

CNC code generation was initially attempted using commercial software, but it was apparent after several attempts that the algorithms and controls available on several software applications were not suitable for the methodology required to create riblets of such small dimensions. Manual generation of CNC code was performed using Microsoft Excel and a pattern of incrementing the X and Y movements in an alternating fashion to cut each riblet with only one mill pass on either side of the riblet. Each riblet surface was milled with one of three different diameters of endmill purchased for the project, and the selection was optimized for cutting speed and reliability. Endmills of 127  $\mu\text{m}$ , 254  $\mu\text{m}$ , and 281  $\mu\text{m}$  diameters were used, and the diameter of the endmill was taken into account in the creation of the CNC code. Care was taken to prevent certain motions of the mill which would allow the backlash of the machine to introduce slop in the movements. Backlash is the amount of motion the mill must attempt to move before any actual motion takes place, and is caused by the tolerances involved in gear-to-gear and other interfaces in the drivetrain of the control motors. These backlash-inducing motions, which involve any alternating forward and backwards motions, are accepted in the longitudinal direction, but must be avoided in the cross-riblet direction to ensure the tightest tolerance exists in the direction with the thinnest feature of the riblets. Additional care was taken to use a movement pattern that would ensure the use of climb-milling, a milling method

in which the forces generated by the spinning endmill cutting into the surface pull the mill forward. This method of milling is less likely than milling in the alternative direction to introduce lateral forces large enough to break the tall and narrow riblets while cutting.

Mill adjustment is a critical step to ensure proper milling of the riblet surfaces. Two processes are involved and allow for the mill to account for backlash. First, adjustments to the mill were made to reduce backlash as much as possible. Additionally, using a dial indicator, it is possible to measure the backlash in each direction by making alternating forward and backward movements in that direction. When backlash is known, the backlash values can be entered into the mill, which will then account for it automatically to help ensure tighter tolerances. As important as mill adjustment is test piece setup. For this reason, a sacrificial test-piece was first used to ensure the cut of the endmill would correctly mill the riblets without breaking them due to a flaw in any part of the setup of CNC design. Again using a dial indicator, the surface was clamped to the mill with paper shims placed iteratively until the surface of the test piece was flat within several thousandths of an inch. Due to the 0.008 in (203  $\mu\text{m}$ ) cut depth of the smallest endmill, it was critical that the surface flatness profile was known. Cutting deeper than the teeth with even a small endmill results in either a broken endmill bit or a poor surface finish, either of which would render the test piece unusable. After the sacrificial test piece was setup appropriately, test riblets were milled. Many times, adjustments were required in the CNC code or to the mill to ensure that riblets were successfully cut, and again an iterative process proved to be the best approach to ensuring proper riblet milling

on the final test pieces. After milling several riblets into the sacrificial test piece successfully, the final test piece was setup and milled according to the same process as above. During milling a low-velocity stream of air was used to clear chips of acrylic from the milling interface, and upon completion of the entire two-pass test piece milling, a soft bristle brush was used to carefully clean the remaining chips.

### **3.2 Experimental Results and Discussion**

The following results of the riblet drag reduction studies performed are presented as plots of pressure drop across the test section vs.  $s^+$  or Reynolds number and compare riblet test surfaces to flat plate control surfaces. The intended presentation of the results of this study was to be a series of plots of percentage drag reduction vs.  $s^+$  or Reynolds number. However, the lack of measurable pressure drop reduction and relative magnitudes of measured pressure drop across the riblet and flat plate surfaces made interpreting the effects of riblets difficult in that format. A more valuable representation of the results of this study is afforded by plotting as stated above, allowing the direct comparison of pressure drop trends across riblet and flat plate surfaces. The results are presented in that manner below.

A comparison of the pressure drop measured across flat plate and all riblet surfaces of the first test set, with  $h/s$  ratios of 0.3, 0.5, and 0.7, tested in both 4 cm wide and 3 cm wide channels is shown plotted vs. Reynolds number in figure 20. It is apparent from the results presented using the 4 cm channel that in the turbulent regime, no overall beneficial trend is demonstrated for any  $h/s$  ratio or Reynolds number.

Additionally, the results in the 3 cm channel show no overall trend of riblet benefit in the turbulent regime. It is well-demonstrated in the 3 cm channel that the rate at which the pressure drop measured across each riblet surface trends away from the flat plate measurements varies with the  $h/s$  ratio. For clarity and ease of discussion, individual plots are provided which show pressure drop vs.  $s^+$  for both the 4 cm channel and the 3 cm channel (Fig. 21). For all plots in both the 4 cm and 3 cm channels, a notable increase in the pressure drop trendline

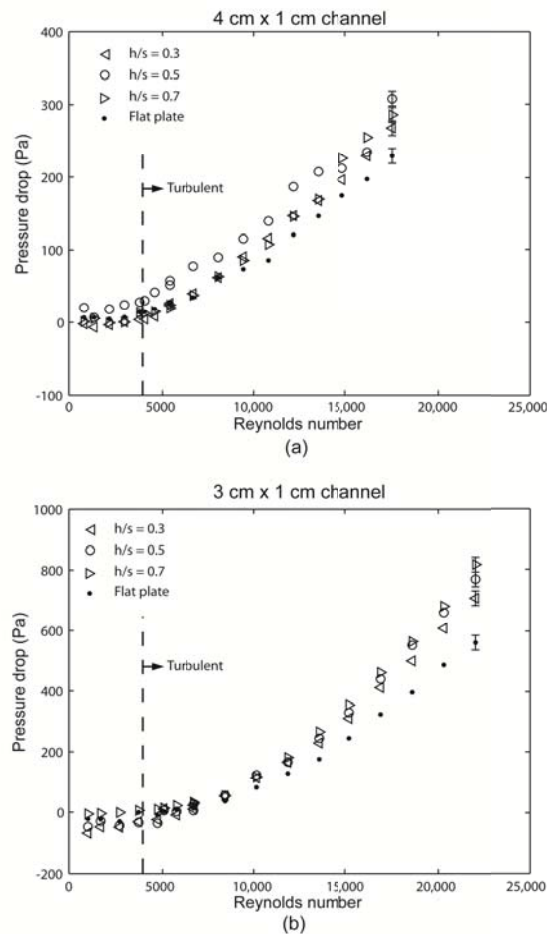


Figure 20. Pressure drop comparison over riblet surfaces with various  $h/s$  ratios and flat plate surfaces in a (a) 4cm x 1cm channel and (b) 3cm x 1cm channel.

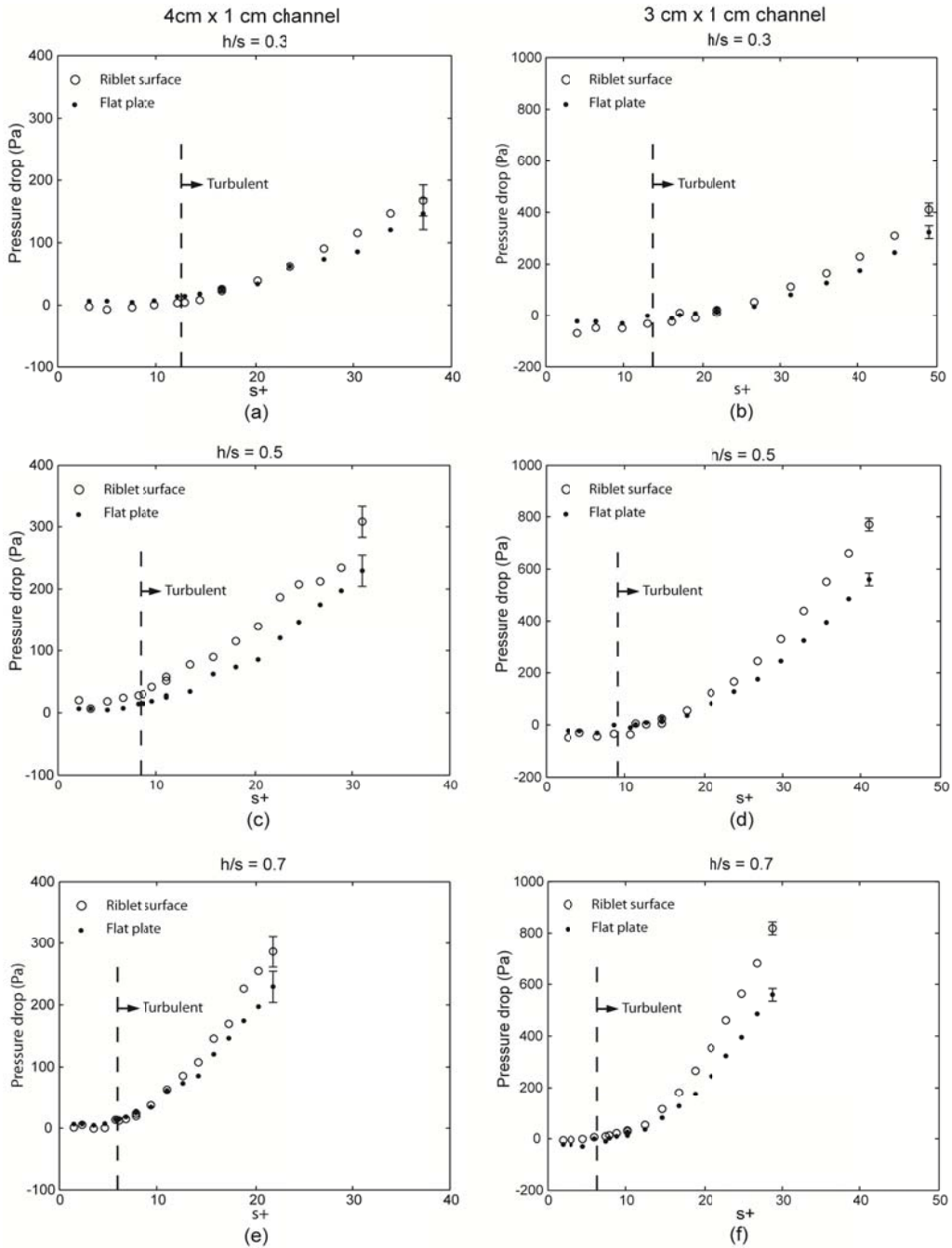


Figure 21. Pressure drop comparison over  $h/s = 0.3$  riblets and flat plate surface in a (a) 4 cm x 1 cm channel and (b) 3 cm x 1 cm channel. Pressure drop comparison over  $h/s = 0.5$  riblets and flat plate surface in a (c) 4 cm x 1 cm channel and (d) 3 cm x 1 cm channel. Pressure drop comparison over  $h/s = 0.7$  riblets and flat plate surface in a (e) 4 cm x 1 cm channel and (f) 3 cm x 1 cm channel.

for riblet surfaces can be seen at an  $s^+$  range of 20 to 25. For riblets in the turbulent range with an  $h/s$  ratio of 0.3, the lowest increase in drag occurs at  $s^+$  values less than 20.

Though no drag-reduction occurs, this trend of lower drag increase is similar to what has been demonstrated in external flows. For riblets with an  $h/s$  ratio of 0.5, a similar trend is seen, but instability of the data makes conclusions difficult to draw in the 4 cm channel, even after numerous measurements were taken on the system. Similar performance is seen again for riblets with an  $h/s$  ratio of 0.7, with an increase in pressure drop occurring at or near an  $s^+$  value of 20.

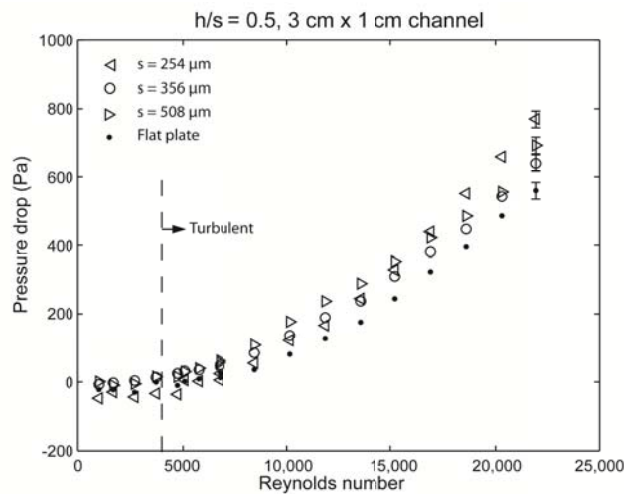


Figure 22. Pressure drop comparison over flat plate surface and riblets with  $h/s = 0.5$  and varied riblet spacing in a 3cm x 1cm channel.

A comparison of the pressure drop measured across flat plate and riblet surfaces of the second test set, with  $h/s$  ratios of 0.5 and dimensional spacings of 254  $\mu\text{m}$ , 356  $\mu\text{m}$ , and 508  $\mu\text{m}$ , tested in the 3 cm channel is shown plotted vs. Reynolds number in figure 22. It is again apparent that in the turbulent regime, no overall trend of drag reduction benefit is demonstrated which is greater than the apparent error of the system

demonstrated by the negative pressure drop measurements seen in the lower Reynolds number data points. Plots of the pressure drop of each individual riblet surfaces compared with the flat plate surface are shown in figure 23. For both sets of smaller riblets, with spacing of 254  $\mu\text{m}$  and 356  $\mu\text{m}$ , a nearly constant increase in pressure drop as compared to the flat plate surface is seen. However, for the riblet surface with spacing of 508  $\mu\text{m}$ , which was tested with the first test set as well, the riblets demonstrate nearly even performance with the flat plate surface until  $s^+$  reaches values greater than 20.

While the lack of pressure drop and drag reduction benefit in these studies appears to show that riblets do not operate in the expected manner in a rectangular duct of these dimensions and flow characteristics, there is evidence in the data to show that this is not the case. With a null-assumption that riblets increase surface roughness and provide no drag-reduction benefit, a more constant trend of increased drag would be expected. A reduction in this expected increase in drag reduction is shown only in the expected range of  $s^+$ , which is evidence of some effect of the riblets, and in turn a high-level confirmation of the presence of streamwise vortices which behave in a similar manner as those known to exist in external flows. Though there is this evidence of some minor riblet benefit occurring, the overall detrimental effects of the riblets must be accounted for. Several factors may be coming together to prohibit the expected benefits of the riblets, including the irregular flow behavior in the rectangular duct, riblet-to-channel size ratio considerations, magnitude of surface roughness resulting from the milling as compared to the riblet and channel dimensions, and also the development of the flow throughout the channel.

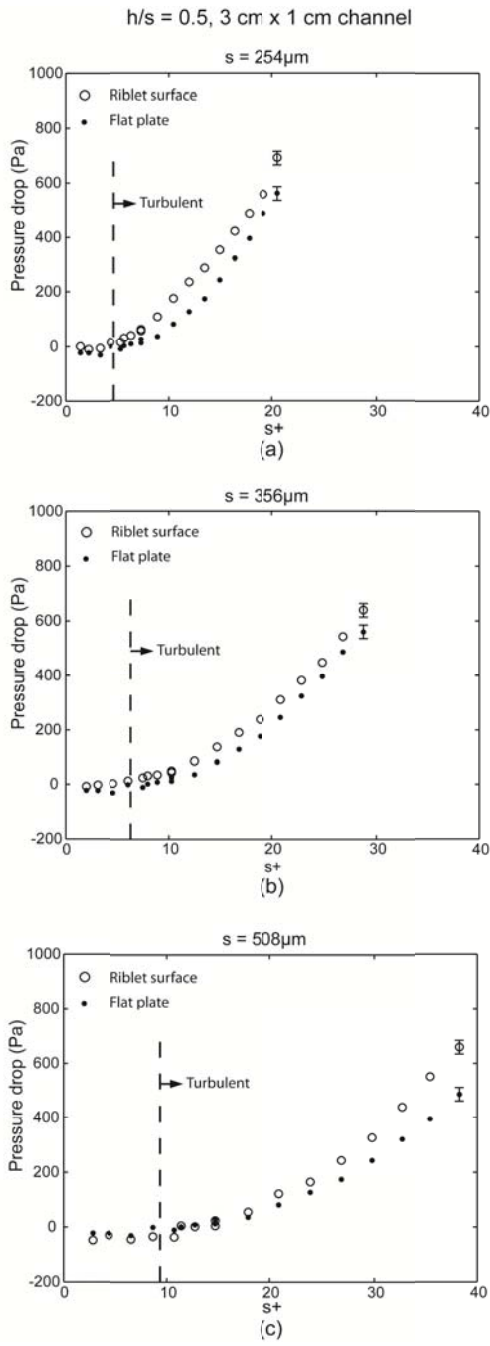


Figure 23. (a) Pressure drop comparison over  $h/s = 0.5$  riblets with  $254\mu\text{m}$  spacing and flat plate surface in a 3cm x 1cm channel. (b) Pressure drop comparison over  $h/s = 0.5$  riblets with  $356\mu\text{m}$  spacing and flat plate surface in a 3cm x 1cm channel. (c) Pressure drop comparison over  $h/s = 0.5$  riblets with  $508\mu\text{m}$  spacing and flat plate surface in a 3cm x 1cm channel.

One of the key flow-modifications of riblet surfaces is the reduction in ejection of the streamwise vortices which form in the viscous sublayer. Though benefit was seen in external-flow studies and internal round-pipe flow studies, the structure and behavior of the vortices as well as the interactions between the vortices is not as predictable or uniform in rectangular duct flow. On an infinite flat plate or a smooth round pipe, vortices all are free to form and eject from the surface in a somewhat continuous and regular pattern. With no sharp edges affecting the formation or ejection direction of the vortices, the riblets can function as expected across the entire surface. In rectangular duct flow, however, the adjacent walls of the channel may allow vortices to eject directly across a riblet surface, effectively disrupting the ability of the riblets to pin vortices and keep them from interacting and ejecting into the bulk flow. Similarly, the bulk formation of general turbulence behavior caused by fluid interactions with the corners at the adjacent walls may cause pressure differentials to exist near the edge of the riblet section causing the outer-most vortices to lose any stability created by the riblet structures.

While the riblets near the corners may be extraneous due to the interactions of the adjacent boundary layer interactions, there are three major surfaces in this flow channel which were not covered in riblets and aren't able to reduce the probability of vortex ejection. This may also have a negative effect on the system. If it possible that without limiting the ejection of the vortices from the opposing surface in the channel, bulk flow turbulence behavior exists in such a way or at such an intensity level that it can disrupt any beneficial behavior of the test riblet section by creating pressure differentials which negate the pinning effect that the riblet have on the vortices. Similarly, the ejection of

vortices from the adjacent walls afforded by the lack of riblet coverage may allow vortex ejection which again causes pressure differentials to exist above and across the riblet section that serve to negate the riblet functions in a similar manner.

Several dimensional considerations may also cause a decrease in performance of the system. It is feasible that the dimensions of the riblet channel are not great enough to warrant the application of riblets. That is, the expected formations and interactions of the streamwise vortices may occur, but the ejection behavior is diminished or somehow altered by pressure patterns or interactions within the fluid of the system. When compared to an external flow, the ratio of riblet protrusion height into the flow vs. thickness of flow field is much higher. In external flows the flow field may be approximated as infinitely thick, while in this duct flow the flow field is limited in all directions. It is possible that the protrusion height of the riblets decreases the cross-sectional area of the flow field to a large enough extent that the riblet effects are unable to overcome the negative effects of the flow field reduction. To provide benefit above that of a flat plate duct which is smooth and without impeding surface features, the riblets would have to provide much greater benefit than in external flows. Riblets which are used in external flows protrude into the flow as well, but the percentage decrease in flow area for fluid over an external riblet surface is much less than the percentage decrease in flow area for fluid over an internally placed riblet surface.

An additional dimensional consideration that may cause a decrease in performance is the magnitude of the roughness effects inherent to the fabrication processes used on the system vs. the riblet size. Thin riblets with sharp, smooth tips are

ideal for drag reduction benefit, as discussed in previous works (Bechert, 1997b). Shown above in figure 19, it is apparent that surface roughness exists at a scale which may be detrimental to the system behavior. At the smallest riblet sizes tested in the second test set,  $h/s = 0.5$  with spacings of  $s = 254 \mu\text{m}$  and  $356 \mu\text{m}$ , it is seen that a nearly constant increase in pressure drop compared to the flat plate surface is measured across the test section at all values of  $s^+$ . This may indicate that the behavior of the riblets is completely negated by the effects of this roughness on the smallest riblets manufactured.

## CHAPTER 4:

### SUMMARY

The mechanisms of fluid drag were discussed, and the presence of streamwise vortices on the surface during turbulent flow was established. An introduction and review of the current state of understanding of the mechanisms by which shark skin inspired riblets function to reduce the drag experienced in turbulent flow was given. Data was presented which demonstrates optimized performance of various riblet geometries and arrangements, and a discussion of the benefits of mucus and hydrophobic surfaces were presented with suggestions for further study.

A flow cell was designed such that the effects of riblets in turbulent, internal rectangular duct flow could be studied. The flow cell and experimental procedure were designed to allow for experimentation on multiple families of riblet surfaces without major changes to the flow cell. Riblets were fabricated which protruded into the flow using a small-scale CNC mill, which allowed the reliable production of blade-style riblet surfaces. Protrusion into the flow as well as roughness left by the milling process may be key factors in the lack of overall drag reduction produced by the riblets. The data collected and presented demonstrates that for certain, expected values of  $s^+$ , there is not overall benefit, but rather there is less detrimental pressure drop increase as compared to the general trend of pressure drop increase caused by riblet surfaces. For this reason, it is concluded that riblets surfaces as presented in this paper, while not beneficial in duct

flow of this nature and dimensional characteristics, do show expected trends and may show more benefit with further study in internal rectangular duct flow.

To further understand the possible benefit of riblets in rectangular ducts, future studies should be performed on rectangular ducts with various aspect ratios using computer simulation or flow visualization techniques. By first achieving a better understanding of the structure and behavior of the turbulent boundary layer on surfaces and at the corners where adjacent surfaces meet by using these simulation and visualization techniques, one would be more able to study and understand the applicability of riblets in rectangular duct flow.

## LIST OF REFERENCES

- Bechert D.W. and Hoppe G., 1985, "On the Drag Reduction of the Shark Skin," Paper # AIAA-85-0564, presented at AIAA Shear Flow Control Conference, Boulder, CO, March 12-14.
- Bechert D.W., Bartenwerfer M., Hoppe G., and Reif, W.-E., 1986, "Drag reduction mechanisms derived from shark skin," Paper # ICAS-86-1.8.3, presented at 15<sup>th</sup> Congress of the International Council of Aeronautical Sciences, London, UK, Sept. 7-12.
- Bechert D.W., Hoppe G., van der Hoven J.G.Th., and Makris R., 1992, "The Berlin oil channel for drag reduction research," *Exper. Fluids* **12**, 251-260.
- Bechert D.W., Bruse M., Hage W., and Meyer R., 1997a, "Biological surfaces and their technological application – laboratory and flight experiments on drag reduction and separation control," Paper # AIAA-1997-1960, presented at AIAA 28<sup>th</sup> Fluid Dynamics Conference, Snowmass Village, CO, June 29-Aug 2.
- Bechert D.W., Bruse M., Hage W., Van Der Hoeven J.G.T., and Hoppe G., 1997b, "Experiments on drag reducing surfaces and their optimization with an adjustable geometry," *J. Fluid Mech.* **338**, 59-87.
- Bechert D.W., Bruse M., and Hage W., 2000a, "Experiments with three-dimensional riblets as an idealized model of shark skin," *Exper. Fluids* **28**, 403-412.
- Bechert D.W., Bruse M., Hage W., and Meyer, R., 2000b, "Fluid mechanics of biological surfaces and their technological application," *Naturwissenschaften* **87**, 157-171.
- Bhushan B., 2007, "Adhesion of Multi-level Hierarchical Attachment Systems in Gecko Feet," (invited), *J. Adhesion Sci. Technol.* **21**, 1213-1258.
- Bhushan B., 2008, *Nanotribology and Nanomechanics – An Introduction, second edition*, Springer-Verlag, Heidelberg, Germany.
- Bhushan, B., 2009, "Biomimetics: lessons from nature—an overview," *Phil. Trans. R. Soc. A* **367**, 1445-1486.
- Bhushan B., 2010, *Springer Handbook of Nanotechnology, third edition*, Springer-Verlag, Heidelberg, Germany.
- Bhushan, B and Her, E. K., 2010, "Fabrication of Superhydrophobic Surfaces with High and Low Adhesion Inspired from Rose Petal," *Langmuir* **26**, 8207-8217.

- Choi K.S., Gadd G.E., Pearcey H.H., Savill A.M., and Svensson S., 1989, "Tests of drag-reducing polymer coated on a riblet surface," *Appl. Sci. Res.* **46**, 209-216.
- Choi K.S., Yang X., Clayton B.R., Glover E.J., Altar M., Semenov B.N., Kulik V.M., 1997, "Turbulent drag reduction using compliant surfaces," *Proc. R. Soc A* **453**, 2229-2240.
- Coles D., 1978, "A model for flow in the viscous sublayer," Proceedings of the Workshop on Coherent Structure of Turbulent Boundary Layers, Bethlehem, PA, 462-475.
- Cutkosky, M.R., and Kim S., 2009, "Design and fabrication of multi-material structures for bioinspired robots," *Phil. Trans. R. Soc. A* **367**, 1799-1813.
- Daniel T.L., 1981, "Fish mucus: *in situ* measurements of polymer drag reduction," *Biological Bulletin* **160**, 376-382.
- Dean B.D. and Bhushan B., 2010 "Shark-skin surfaces for fluid-drag reduction in turbulent flow: a review," *Phil. Trans. R. Soc. A* **368**, 4775-4806.
- Denkena B., Leon, L.de, and Wang B., 2009, "Grinding of microstructures functional surfaces: a novel strategy for dressing of microprofiles," *Prod. Eng.* **3**, 41-48.
- Enyutin G.V., Lashkov Yu A., and Samoilova N.V., 1995, "Drag reduction in riblet-lined pipes," *Fluid Dynamics* **30**, 45-48.
- Frings B., 1988, "Heterogeneous drag reduction in turbulent pipe flows using various injection techniques," *Rheologica Acta* **27**, 92-10.
- Goldstein D., Handler R., and Sirovich L., 1995, "Direct numerical simulation of turbulent flow over a modeled riblet covered surface," *J. Fluid Mech.* **302**, 333-376
- Gorb, S., 2001, *Attachment Devices of Insect Cuticles*, Kluwer, Dordrecht, Netherlands.
- Han M., Huh J.K., Lee S.S., and Lee S., 2002, "Micro-riblet film for drag reduction," Proceedings of the Pacific Rim Workshop on Transducers and Micro/Nano Technologies, Xiamen, China.
- Hoyt J.W., 1975, "Hydrodynamic drag reduction due to fish slimes," *Swimming and Flying in Nature* **2**, 653-672.
- Jung Y.C. and Bhushan, B., 2010, "Biomimetic structures for fluid drag reduction in laminar and turbulent flows," *J. Phys.: Condens. Matt.* **22**, 035104.

Kline, S.J., Reynolds W.C., Schraub F.A., and Runstadler P.W., 1967, "The structure of turbulent boundary layers," *J. Fluid Mech.* **30**, 741-773.

Klocke F., Feldhaus B., and Mader S., 2007, "Development of an incremental rolling process for the production of defined riblet surface structures," *Prod. Eng.* **1**, 233-237.

Koury E., and Virk P.S., 1995, "Drag reduction by polymer solutions in a riblet-lined pipe," *Appl. Sci. Res.* **54**, 323-347.

Krieger K., 2004, "Do pool sharks really swim faster?" *Science*, **305**, 636-637.

Lang A.W., Motta P., Hidalgo P., and Westcott M., 2008, "Bristled shark skin: a microgeometry for boundary layer control?" *Bioinspiration and Biomimetics* **3**, 1-9.

Lee S.J. and Choi Y.S., 2008, "Decrement of spanwise vortices by a drag-reducing riblet surface," *J. Turbulence* **9**, 1-15.

Lee S.-J., and Lee S.-H., 2001, "Flow field analysis of a turbulent boundary layer over a riblet surface," *Exp. Fluids* **30**, 153-166

Liu K.N., Christodoulou C., Riccius O., and Joseph D.D., 1990, "Drag reduction in pipes lined with riblets," *AIAA Journal* **28**, 1697-1699

Marentic F.J. and Morris T.L., 1992, "Drag reduction article," United States Patent, No. 5,133,516.

Munson B., Young D., and Okiishi T., 2005, *Fundamentals of Fluid Mechanics*, 5<sup>th</sup> ed., Wiley, New York.

Nosonovsky M. and Bhushan B., 2008, *Multiscale Dissipative Mechanisms and Hierarchical Surfaces: Friction, Superhydrophobicity, and Biomimetics*, Springer-Verlag, Heidelberg, Germany.

Ou, J, Perot B., and Rothstein J.P., 2004, "Laminar drag reduction in microchannels using ultrahydrophobic surfaces," *Phys. Fluids* **16**, 4635-4643.

Reif W.-E., 1985, *Squamation and Ecology of Sharks*, Courier Forschungsinstitut Senckenberg, Frankfurt, Germany, **78**, 1-255.

Robinson S.K., 1991, "The kinematics of turbulent boundary layer structure," NASA TM 103859, NASA, Washington, DC.

Rohr J.J., Anderson G.W., Reidy L.W., and Hendricks E.W., 1992, "A comparison of the drag-reducing benefits of riblets in internal and external flows," *Exp. Fluids*, **13**, 361-368.

- Shephard K.L., 1994, "Functions for fish mucus," *Rev. Fish Biology and Fisheries* **4**,401-429.
- Walsh M.J., 1980, "Drag characteristics of v-groove and transverse curvature riblets," *Viscous Flow Drag Reduction* **72**, 169-184.
- Walsh M.J., 1982, "Turbulent boundary layer drag reduction using riblets," Paper # AIAA-82-0169, presented at AIAA 20<sup>th</sup> Aerospace Sciences Meeting, Orlando FL, Jan 11-14.
- Walsh M.J., and Anders J.B., 1989, "Riblet/LEBU research at NASA Langley," *Appl. Sci. Res.* **46**, 255-262.
- Walsh M.J. and Lindemann A.M., 1984, "Optimization and application of riblets for turbulent drag reduction," Paper # AIAA-84-0347, presented at AIAA 22<sup>nd</sup> Aerospace Sciences Meeting, Reno, NV, Jan 9-12.
- Weiss M.H., 1997, "Implementation of drag reduction techniques in natural gas pipelines," presented at 10<sup>th</sup> European Drag Reduction Working Meeting, Berlin, Germany, March 19-21.
- Wilkinson S.P., 1983, "Influence of wall permeability on turbulent boundary-layer properties," Paper # AIAA 83-0294, presented at 21<sup>st</sup> Aerospace Sciences Meeting of the American Institute of Aeronautics and Astronautics, Reno, NV, Jan 10-13.
- Wilkinson S.P., and Lazos B.S., 1987, "Direct drag and hot-wire measurements on thin-element riblet arrays," presented at the IUTAM Symposium on Turbulence Management and Relaminarization, Bangalore, India, Jan 19-23.
- Wilkinson S.P., Anders J.B., Lazos B.S., and Bushnell D.M., 1988, "Turbulent drag reduction research at NASA Langley: progress and plans," *Inter. J. Heat and Fluid Flow* **9**, 266-277.
- Xin H., and Zhang D, 2008, "Study on the micro-replication of shark skin," *Science in China Series E: Technological Sciences* **51**, 890-896.